Detection and Identification of the Keto-Hydroperoxide ($HOOCH_2OCHO$) and other Intermediates during Low-Temperature Oxidation of Dimethyl Ether

Kai Moshammer[1,2], *Ahren W. Jasper*[1], *Denisia M. Popolan-Vaida*[3], *Arnas Lucassen*[1†], *Pascal Dievart*[4], *Hatem Selim*[5], *Arkke J. Eskola*[1], *Craig A. Taatjes*[1], *Stephen R. Leone*[3], *S. Mani Sarathy*[5], *Yiguang Ju*[4], *Philippe Dagaut*[6], *Katharina Kohse-Höinghaus*[2], *Nils Hansen*[1,*]

[1]Combustion Research Facility, Sandia National Laboratories, Livermore, CA 94551, USA

[2]Department of Chemistry, Bielefeld University, D-33615 Bielefeld, Germany

[3]Departments of Chemistry and Physics, University of California, Berkeley, CA 94720, and Chemical Sciences Division, Lawrence Berkeley National Laboratory, Berkeley, CA 94720

[4]Department of Mechanical and Aerospace Engineering, Princeton University, Princeton, NJ 08544, USA

[5]Clean Combustion Research Center, King Abdullah University of Science and Technology, Thuwal 23955-6900, Saudi Arabia

[6]Centre National de la Recherche Scientifique (CNRS), INSIS, Orléans Cedex 2, France

submitted to:

J. Phys.Chem. A

31 Pages

12 Figures

3 Tables

Supplementary Material is available.

[†] Present address: Department of Thermophysical Properties, Physikalisch-Technische Bundesanstalt, D-38116 Braunschweig, Germany

[*] Corresponding author: email: nhansen@sandia.gov; Tel.: 001-925-294-6272; Fax: 001-925-294-2276

Abstract

In this paper we report the detection and identification of the keto-hydroperoxide (hydroperoxymethyl formate, HPMF, $HOOCH_2OCHO$) and other partially oxidized intermediate species arising from the low-temperature (540 K) oxidation of dimethyl ether (DME). These observations were made possible by coupling a jet-stirred reactor with molecular-beam sampling capabilities, operated near atmospheric pressure, to a reflectron time-of-flight mass spectrometer that employs single-photon ionization via tunable synchrotron-generated vacuum-ultraviolet radiation. Based on experimentally observed ionization thresholds and fragmentation appearance energies, interpreted with the aid of *ab initio* calculations, we have identified HPMF and its conceivable decomposition products HC(O)O(O)CH (formic acid anhydride), HC(O)OOH (performic acid), and HOC(O)OH (carbonic acid). Other intermediates that were detected and identified include $HC(O)OCH_3$ (methyl formate), *cycl.*-CH_2-O-CH_2-O- (1,3-dioxetane), CH_3OOH (methyl hydroperoxide), HC(O)OH (formic acid), and H_2O_2 (hydrogen peroxide). We show that the theoretical characterization of multiple conformeric structures of some intermediates is required when interpreting the experimentally observed ionization thresholds, and a simple method is presented for estimating the importance of multiple conformers at the estimated temperature (~100 K) of the present molecular beam. We also discuss possible formation pathways of the detected species: For example, supported by potential energy surface calculations, we show that performic acid may be a minor channel of the $O_2 + \dot{C}H_2OCH_2OOH$ reaction, resulting from the decomposition of the $HOOCH_2O\dot{C}HOOH$ intermediate, which predominantly leads to the HPMF.

1. Introduction

The low-temperature oxidation of dimethyl ether (DME) receives continuous attention in the combustion community and many experimental, theoretical, and modeling studies have been reported.[1-25] The motivation for these efforts has been varied: Because innovative engine designs like homogeneous charge compression ignition (HCCI) engines rely on the control of low temperature ignition timing,[26-27] it becomes increasingly necessary to explore the low-temperature combustion (LTC) of transportation fuels. DME has been proposed as an alternative and/or additive to conventional Diesel fuel and it is of particular interest because it has a high cetane number (≥ 55), low soot emission characteristics, and interesting physical-chemical properties (such as a low boiling point, easy liquefaction under pressure, and photochemical inertness).[28-30] Also, it can be massively produced from both biomass and from fossil fuel reforming. DME represents the simplest molecular structure (CH_3OCH_3) with rich low-temperature chemistry and the recent experiments with advanced diagnostics clearly showed that the description of DME's low-temperature chemistry has a large uncertainty in the decomposition pathways and/or the branching ratio of the keto-hydroperoxide species.[18, 22, 25]

Given its great application potential and the simplicity in molecular structure, the high-temperature combustion chemistry of DME has also been extensively studied.[31-47] Because of the importance of low-temperature chemistry in determining fuel effects in autoignition, the present paper focuses on the key reactions and intermediates of the low-temperature regime, and the results of the high-temperature chemistry studies will not be reviewed here.

Over the years, several models have been developed to predict the distinct low-temperature chemistry of DME. Most of these models can be traced back to the one by Curran *et al.*,[3] which was designed to simulate the oxidation of DME in a shock-tube and a jet-stirred

reactor over the temperature range of 650–1300 K. This model, which includes both low- and high-temperature chemistry of DME, was able to predict properly the total ignition delay time and concentration profiles for the products. Later, Curran *et al.*[6] performed further reactor experiments and improved the model performance over a broad temperature range. Recently, various follow-up models that include updated elementary rate coefficients or thermodynamic data have been proposed.[16, 24-25, 47-48]

According to these models, at low temperatures O_2 can add to the $CH_3O\dot{C}H_2$ radical after the initial H-atom abstraction from DME to form an energetically excited methoxymethylperoxy radical ($CH_3OCH_2O\dot{O}$*), which can stabilize (R1), isomerize (R2), or decompose via reactions (R3 and R4):

$$CH_3O\dot{C}H_2 + O_2 \rightleftarrows CH_3OCH_2O\dot{O}^* \rightleftarrows CH_3OCH_2O\dot{O} \quad \text{(R1)}$$

$$\rightleftarrows \dot{C}H_2OCH_2OOH \quad \text{(R2)}$$

$$\rightleftarrows \textit{cycl.}\text{-}CH_2\text{-}O\text{-}CH_2\text{-}O\text{-} + OH \quad \text{(R3)}$$

$$\rightleftarrows 2\ CH_2O + OH \quad \text{(R4)}$$

For a better visual description of the oxidation steps of dimethyl ether at low temperatures a schematic diagram is provided in Figure 1. The stabilized $CH_3OCH_2O\dot{O}$ radical can react with HO_2 or abstract an H-atom from another molecule to form peroxides:

$$CH_3OCH_2O\dot{O} + HO_2 \text{ (or RH)} \rightleftarrows CH_3OCH_2OOH + O_2 \text{ (or } \dot{R}\text{)} \quad \text{(R5)}$$

The O-O bond in the hydroperoxide can easily break to form two radicals:

$$CH_3OCH_2OOH \rightleftarrows CH_3OCH_2\dot{O} + OH, \quad \text{(R6)}$$

thus, reaction (R6) provides a source of chain-branching in low-temperature oxidation (not shown in Fig. 1).

The reaction (R4) is supposed to be more important at temperatures above ~600 K when the stabilized $CH_3OCH_2O\dot{O}$ radical becomes thermally unstable. At lower temperatures further chain-branching can occur depending on the availability of the $\dot{C}H_2OCH_2OOH$ radical, which is expected to have a long lifetime at low temperatures and high pressures.[49] A second O_2 addition then leads to the formation of $\dot{O}OCH_2OCH_2OOH$, which rapidly isomerizes or dissociates (see Figure 1 for a schematic representation):

$$\dot{C}H_2OCH_2OOH + O_2 \rightleftarrows \dot{O}OCH_2OCH_2OOH \quad \text{(R7)}$$

$$\rightleftarrows HOOCH_2O\dot{C}HOOH \quad \text{(R8)}$$

$$\rightleftarrows HOOCH_2OCHO + OH \quad \text{(R9)}$$

$$\rightleftarrows \dot{O}CH_2OCHO + OH + OH \quad \text{(R10)}$$

$$\rightleftarrows \dot{C}H_2OCHO + HO_2 + OH \quad \text{(R11)}$$

Reaction (R9) forms the keto-hydroperoxide $HOOCH_2OCHO$ (hydroperoxymethyl formate, HPMF) which can decompose to the carbonyl-hydroperoxide radical ($\dot{O}CH_2OCHO$) and another OH radical. Consequently, the reactivity of the system increases by providing another possible chain-branching reaction. In fact this kind of chain-branching reaction is thought to dominate in the low-temperature oxidation of many other fuels,[50-52] thus making DME an excellent model system to study low-temperature chemical reaction schemes.

In this study we provide further experimental evidence for the proposed low-temperature oxidation scheme and unprecedentedly detailed information about the intermediate composition during these processes in general. For example, we report the detection and identification of the HPMF, its decomposition products, and many other intermediates including hydroperoxides. The new insights reported herein were made possible through a rigorous combination of *ab-initio* calculations with high-resolution mass-spectrometric data obtained via molecular-beam sampling from a jet-stirred reactor operated near atmospheric pressure. Key to the experiments was the use of single-photon ionization by synchrotron-generated tunable vacuum-ultraviolet (VUV) radiation that allowed for identification of the species and their fragments by their characteristic ionization thresholds. The theoretical calculations provided guidance on how to interpret the data, which can be largely influenced by the conformeric composition in the cold molecular beam.

The current qualitative measurements of intermediate species reported in this publication are helpful for the understanding of the low-temperature oxidation processes of transportation fuels in general and of DME in particular. The experimental and theoretical approaches are described in more detail in the following Section.

2. Experimental and Theoretical Approaches

2.1. Experiment

Low-temperature oxidation processes are often studied using jet-stirred reactor (JSR) and flow reactor systems. Typically, these studies provide mole fractions of reactants, intermediates and products measured at the outlet of the reactor as a function of different parameters such as temperature, pressure, residence time or inlet gas composition, which can then be used to guide

the development and to validate combustion chemistry models.[53] For the identification and quantification of the molecular components, the JSR systems are predominantly coupled to gas chromatographs but cavity-ringdown spectroscopy,[54-57] infrared spectroscopy,[58] and mass spectrometry[18, 59-65] have also been applied to analyze the gas mixture. Especially when combined with molecular-beam sampling, mass spectrometry provides a powerful analytical tool for studying the composition of many gas-phase reaction systems as it allows for simultaneous detection of virtually all species, including radicals, without prior knowledge of their chemical identity.[66-67]

In this study we coupled a jet-stirred reactor, consisting of a fused silica sphere, to a high-resolution time-of-flight molecular-beam mass spectrometer (Fig. 2) that relies on tunable synchrotron-generated vacuum ultraviolet (VUV) radiation for photoionization (PI).

The experiments were performed at Terminal 3 of the Chemical Dynamics Beamline of the Advanced Light Source at the Lawrence Berkeley National Laboratory where we utilized the high flux (10^{14} photons/s) and very good energy resolution [$E/\Delta E$(FWHM) ~ 250-400] of the photon beam in the chemically interesting region from 7.4-30 eV.[68] One of the key features of this experimental set-up is the recording of photoionization efficiency (PIE) curves by scanning the photon energy, which enables the detection of isomer-specific ionization thresholds for a given mass-to-charge (*m/z*) ratio. An important assumption is that only single-charge ions are formed. Additionally, the molecular-beam sampling capability of the JSR allows for the detection of highly reactive compounds like peroxides.

The volume of the jet-stirred reactor is about 33.5 cm^3. Gas streams of DME and oxygen (diluted with argon) were guided through two concentric tubes, mixing at their outlets. The mixed gases then enter the reactor through 4 injectors with exit nozzles located in the center of

the JSR. The four nozzles, which each have an inner diameter of about 1 mm, form the stirring jets. The gas flows were regulated by calibrated (against N_2) mass flow controllers (MKS) with an error of less than 5%. Appropriate gas conversion factors were applied for O_2, Ar, and DME. The reactor is completely enclosed by an oven that allows for adjusting the temperature over the desired range. The oven and the reactor are surrounded by a water-cooled stainless steel chamber. Exhaust gases are continuously removed to keep the pressure constant. The temperature was measured with a thermocouple (K-type, Thermocoax) within the vicinity of the sampling location.

The reaction gases were sampled out of the reactor and guided into the molecular-beam mass spectrometer through a quartz nozzle with a 40° cone angle and a ~50 μm orifice diameter at the tip. Details of the MBMS part of the instrument have been described elsewhere.[66, 69] Briefly, the apparatus consists of a two-stage differentially pumped vacuum chamber that hosts the ion source of the mass spectrometer. A reduction from near atmospheric pressure in the reactor to ~10^{-3} mbar in the 1st pumping stage leads to the formation of a molecular beam and precludes further reactions. The beam then passes through a skimmer into the ionization region of the mass spectrometer held at 10^{-6} mbar. A custom-built reflectron time-of-flight system was used that has sensitivity in the 1 ppm range, a dynamic range of several orders of magnitude, and a mass resolution of $m/\Delta m$ ~2500. All these properties are required to allow detailed analysis of a complex mixture of oxygenates and hydrocarbons.[69-71]

The results shown in this work were taken from a reactor continuously operated at 540 K in the exhaust gas, at a residence time of 5000 ms, and a constant pressure of 976 mbar. The fuel-to-oxygen ratio in the unburnt gases is characterized by a stoichiometry of 0.35. Energy-

dependent mass spectra were measured in the energy range from 9.5 to 13.5 eV. A typical overview mass spectrum is shown in Fig. 3 for the range of *m/z* = 25-100 u at 11.2 eV.

In order to interpret such mass spectra in appropriate detail and to assign chemical structures based on observed ionization thresholds and fragments' appearance energies, guidance from theoretical chemistry was needed. The theoretical approaches are described next.

2.2. Theory

Adiabatic ionization energies were calculated at the M06-2X/aug-cc-pVTZ level of theory, which we estimate to have an uncertainty of ±0.2 eV. Many calculations were refined at a higher level of theory, where QCISD(T)/CBS//M06-2X/aug-cc-pVTZ energies were approximated via QCISD(T)/aug-cc-pVTZ + MP2/CBS – MP2/aug-cc-pVTZ (all calculated at the M06-2X/aug-cc-pVTZ geometries), with the complete basis set (CBS) limit estimated using a two-point formula[72] and the aug-cc-pVTZ and aug-cc-pVQZ basis sets. This level of theory is labeled ~QCISD(T)/CBS and is very similar to one used previously,[73-76] with an estimated uncertainty of ±0.05 eV. For ionization of doublet species, both singlet and triplet cations were considered, and the adiabatic ionization energy for the lowest-energy cation is reported. The calculated ionization energies are summarized in Table 1. Some cations optimized to partially dissociated structures (e.g., structures with loose HO_2 or O_2 fragments), and these were considered as potential fragmentation channels.

For most of the species considered here, a single adiabatic ionization energy is reported corresponding to the locally adiabatic ionization energy for the lowest-energy conformer of the neutral species. This conformer was determined by performing several optimizations of the neutral species at the M06-2X/cc-pVDZ level of theory with initial guesses generated on a sparse

grid of two or three dihedral angles per torsion. The lowest-energy conformer obtained via these scans was considered exclusively at the higher levels of theory discussed above.

For a few species, a more detailed conformational study was carried out. For these systems, the relevant dihedral angles were sampled uniformly to generate ~1000 initial guesses from which full-dimensional optimizations were performed. Unique conformers were identified based on their energies, rotational constants, and vibrational frequencies. Locally adiabatic ionization energies were calculated for each conformer. Conformer-dependent adiabatic ionization energies may be defined as the energy difference between the ground vibrational state of some conformer of the neutral species and the ground vibrational state of its corresponding locally adiabatic conformer on the cation surface. The locally adiabatic cation conformer is obtained via optimization from a vertical excitation to the cation surface from the neutral conformer equilibrium geometry. Locally adiabatic ionization energies for different conformers can vary significantly, with differences much greater than the assigned uncertainties in the present theoretical approaches.

The relative population of each conformer in the molecular beam was characterized using the non-separable and effective harmonic models, which have been described elsewhere in the context of atomic clusters.[77] Briefly, the local partition functions for each unique conformer were evaluated using the harmonic oscillator and rigid rotor approximations and the local frequencies and rotational constants, with small corrections made for low-frequency vibrational modes.[77] The relative populations of each conformer may be assumed to be proportional to the local partition functions evaluated with a consistent zero of energy. This approach is similar to the low-temperature limit of more sophisticated methods that have been recently developed for calculating anharmonic partition functions.[78] These results are interpreted to predict a

distribution of adiabatic ionization energies given by the locally adiabatic ionization energies of the conformers weighted by their populations. This interpretation implies negligible Franck-Condon factors for excitations to the cation surface with conformational changes other than the locally adiabatic ones, which may be a severe approximation. Furthermore, we have neglected conformer-dependent Franck-Condon factors, and conformer-dependent electronic transition matrix elements, and the method for calculating the populations may include significant uncertainties due to its approximate treatment of anharmonicity. For a complete quantitative analysis of the JSR-sampled photoionization efficiency (PIE) curves and to derive individual conformeric contributions, these effects would need to be taken into account. Nonetheless, this simple approach is readily applied to complex systems and includes the major effects of conformational changes on the calculated adiabatic ionization energy. More detailed calculations are beyond the scope of this work. We primarily consider populations evaluated at 100 K, which is an estimated temperature of the sampled beam. The temperature could be lower based on recent experiments,[79] but it would not drastically change the results. We considered a higher temperature of 250 K to demonstrate the sensitivity of the conformer population on temperature.

Detailed conformer studies were carried out for the keto-hydroperoxide HPMF ($HOOCH_2OCHO$, *m/z* = 92.011 u) and performic acid [HC(O)OOH, *m/z* = 62.000 u]. Multiple conformers with non-negligible populations at the temperatures of the sampled beam (~100 K) were found. We note that the most likely conformers are not necessarily those with the lowest electronic energies, as their relative populations will depend additionally on the local vibrational frequencies and rotational constants.[78] Detailed results for the identification of isomers at *m/z* = 92 u and 62 u are discussed below.

Fragmentation channel energies were calculated at the levels of theory discussed above for several species, and results relevant to the peak assignments discussed below are summarized in Table 2. The fragmentation channel energy is defined as the energy difference between the product fragments and the neutral parent species, where both energies are zero-point inclusive and the lowest-energy conformers are considered. Channel energies are associated with experimentally determined appearance energies but may be lower bounds due to the presence of barriers to dissociation on the cation surface and due to competing fragmentation channels. This issue is discussed in detail in Section 3.2.

3. Results and Discussion

This section is organized as follows: First, we present an overview of the mass-to-charge ratios and their corresponding elemental compositions which will be discussed in this section. Second, we discuss the detection and identification of some intermediates such as CH_2O, H_2O_2, CH_3OOH, and $HC(O)OCH_3$ to provide insights into the mass- and energy-resolving capabilities of the experimental system employed in the current work. Third, we provide further insights into the oxidation process by identifying the keto-hydroperoxide HPMF, its fragments, and its conceivable decomposition products.

As discussed above, Figure 3 shows a mass spectrum that was measured at a photon energy of 11.2 eV. It gives a general overview of all mass-to-charge ratios detected during the experiments. In the analysis of such mass spectra, the observed mass-to-charge ratios must be assigned to certain elemental compositions and maybe even structures. Due to the high mass resolution of the reflectron time-of-flight mass spectrometer the determination of the elemental composition of C/H/O species by their exact mass was possible in the relevant mass range. In

this study, species with up to four oxygen atoms were identified and their elemental compositions, namely CH_2O, H_2O_2, C_2H_6O, CH_4O_2, $C_2H_3O_2$, $C_2H_4O_2$, CH_2O_3, CH_4O_3, $C_2H_3O_4$ and $C_2H_4O_4$ are marked in Fig. 3.

When probing complex systems, like low- and high-temperature combustion processes, it can be challenging to unambiguously identify the source of the observed signal in the mass spectrum: it could be due to the reactants, intermediates, or products of the combustion process including their isomeric contributions from ^{13}C and ^{18}O or it could be due to fragmentation processes of individual components.[66, 69, 80] By experimentally determining and theoretically calculating the ionization energy (IE) of these species and the appearance energy (AE) of their fragments, we are able to interpret the observed mass spectra in significant detail and assign the constitutional formulae to their isomeric structures. As we discuss below, these newly detected species are expected to be key intermediates in the low-temperature oxidation processes of DME. In other words, our data provide experimental evidence for the validity of the general scheme of the low-temperature oxidation mechanisms of DME.

3.1. Detection and Identification of m/z = 29 u, 30 u, 34 u, 46 u, 48 u, and 60 u

Peaks were detected for the exact mass-to-charge ratios m/z = 29.003 u (assigned to the elemental composition of CHO), m/z = 30.011 u (CH_2O), and m/z = 34.005 u (H_2O_2). The JSR-sampled PIE curves for m/z = 30.011 u and 34.005 u are shown in Fig. 4 together with the known ionization energies of formaldehyde and hydrogen peroxide.[81] Obviously the mass peaks can be assigned to due to these chemical structures.

The high mass resolution of the mass spectrometer is evident from the data for the two nominal masses 46 and 48. At mass 46, we observed two peaks when ionizing at 11.7 eV (Fig.

5a). Signal at *m/z* = 46.042 u can easily be assigned to DME (the fuel). The other peak at *m/z* = 46.005 u appears above 11.33 eV, as indicated by the recorded PIE curve (Fig. 5b), and can thus be assigned to formic acid [HC(O)OH].[81] The Criegee intermediate (CH_2OO), which is postulated to be part of the low-temperature combustion of DME,[10, 14, 17] has the same exact mass as formic acid but was not detected in this experiment (IE = 9.98 eV[82]). A possible explanation is that the Criegee intermediate is very reactive and thus could be present only in very low concentrations that might be below the detection limit of the current experiment (ppm range).

The signal at *m/z* = 48 u also shows two peaks, that are *m/z* = 48.021 u with an elemental composition of CH_4O_2 and *m/z* = 48.046 u that can be assigned to the ^{18}O isotopomer of the fuel (Fig. 6a). In principle, two isomeric structures are conceivable for CH_4O_2, *e.g.* methanediol ($HOCH_2OH$) and methyl hydroperoxide (CH_3OOH). The ionization threshold for the latter isomer was calculated to be 9.83 eV (Table 1). As can be seen from the PIE curve of *m/z* = 48.021 u (Fig. 6b) the onset of the curve near 9.85(±0.05) eV matches the calculated IE of methyl hydroperoxide (Table 1) accurately and we can thus identify CH_3OOH based on its ionization energy as an intermediate in the low-temperature DME combustion process. It should be noted that the calculated ionization energy for methanediol lies between 10.33 and 11.00 eV and depends on its conformeric structure. However, because this value is significantly larger than the observed threshold, a more detailed conformer analysis is not provided here.

In general, peroxy radical and hydroperoxide species are expected to be a crucial part of the low-temperature combustion, although not all of them are typically detected in DME oxidation experiments. Current DME models include the CH_3O_2 radical as a species in its low-temperature oxidation. This radical can undergo a simple H-atom addition to form methyl hydroperoxide, which might be detected more efficiently in the experiment due to its higher

stability. Note, that, according to kinetic models, the CH_3O_2 radical is formed through the reaction of CH_3 with O_2. However, in the experiment only a weak CH_3 signal was detected, maybe indicating that CH_3 is not as well detected as in many high-temperature flame studies.[83-85] It is possible that in the current low-temperature experiments CH_3 is mostly captured in the form of CH_3O_2 whereas in the high-temperature flames the $CH_3 + O_2 \rightleftarrows CH_3O_2$ equilibrium strongly favors dissociation back to the reactants.

The resolving power of the VUV radiation enables the detection and identification of isomers. Figure 7 shows the JSR-sampled photoionization efficiency curve for *m/z* = 60.021 u ($C_2H_4O_2$). As can be seen, two isomers can be identified based on their characteristic photoionization efficiency curve and ionization thresholds. Apparently, the dominant intermediate at this mass is methyl formate [$HC(O)OCH_3$] and the agreement between the JSR-sampled and its known photoionization efficiency curve is very good.[86] Methyl formate detection has also been reported by Guo *et al.*[18] and Herrmann *et al.*[21] According to most models, methyl formate can be formed starting with reaction (R1) forming the $CH_3OCH_2O\dot{O}$ radical which can lose OH in a 1-step reaction (R12) or by reaction with another RO_2 radical first then followed by a β-scission (R13):

$$CH_3OCH_2O\dot{O} \rightleftarrows CH_3OCHO + OH \qquad \text{(R12)}$$

$$CH_3OCH_2O\dot{O} + RO_2 \rightleftarrows CH_3OCH_2\dot{O} + O_2 + RO \rightleftarrows CH_3OCHO + H + O_2 + RO \qquad \text{(R13)}$$

$CH_3OCH_2\dot{O}$ can also be formed via reaction (R6).

Additionally, we observed a signal in the PIE curve for *m/z* = 60.021 u, with an apparent ionization threshold at 10.05(±0.05) eV. In order to assign a chemical structure to this signal, we

calculated the ionization energies of various $C_2H_4O_2$ isomers (Table 1). The calculated ionization energy of the *cycl.*-CH_2-O-CH_2-O- isomer (1,3-dioxetane) of 10.08 eV matches the experimentally observed threshold the best. The presence of 1,3-dioxetane is probably a consequence of the chain-propagating reaction (R3). Thus, its detection provides some experimental evidence for the variety of the different reactions of the $CH_3OCH_2O\dot{O}$ radical intermediate.

All these previously discussed species [CHO, CH_2O, H_2O_2, HC(O)OH, CH_3OOH, $HC(O)OCH_3$, and *cycl.*-CH_2-O-CH_2-O-] are anticipated to be part of the low-temperature combustion of DME and are widely discussed in the literature.[6, 16, 18, 25] A more detailed discussion will not be provided here. However, their detection and identification can be seen as proof of a successful experiment that allows the separation of isomeric structures and the detection of reactive species.

3.2. Detection of the Hydroperoxymethyl Formate (HPMF) at m/z *= 92 u and its Fragments at* m/z *= 91 u, 64 u, and 59 u*

A single peak could be detected at the nominal mass of 92 u. Its exact mass was determined to be *m/z* = 92.011 u, which correlates with the elemental composition of $C_2H_4O_4$. It seems plausible that under the experimental conditions this signal can be assigned to the keto-hydroperoxide hydroperoxymethyl formate (HPMF, $HOOCH_2OCHO$), although several different other isomers, including the *cycl.*-$CH_2OOCH(OH)O$- (see Fig. 1), are also conceivable. HPMF is expected to be present and can be formed through the OH radical loss from the $HOOCH_2O\dot{C}HOOH$ radical (R9). HPMF is already included in several models for low-

temperature DME oxidation,[3, 6, 16, 24, 33, 47-48] however until now its existence has not been clearly proven experimentally.

The JSR-sampled PIE curve of *m/z* = 92.011 u is shown in Fig. 8, and an ionization threshold of 9.85(±0.05) eV is visible with a larger increase near 10.0 eV. The calculated ionization energy of the *cycl.*-$CH_2OOCH(OH)O$- intermediate of 9.65eV (Theory II) is below the observed threshold, thus indicating that this isomer may not contribute to the observed PIE curve because of a low detection efficiency towards this species or because it is present only in quantities below the detection limit. The theoretical interpretation of the recorded PIE curve required the consideration of multiple conformeric HPMF structures. Fifteen unique conformers were found theoretically for $HOOCH_2OCHO$. The lowest-energy conformer features a hydrogen bond completing a seven-membered ring, and it has the lowest calculated adiabatic ionization energy (9.67 eV at the ~QCISD(T)/CBS level of theory) of the conformers. The remaining conformers have zero-point inclusive energies within 8 kcal/mol (0.35 eV) of the lowest-energy conformer, with half of the conformers within 3.3 kcal/mol (0.14 eV) of the lowest-energy one. The ionization energies for these fourteen higher-energy conformers vary from 9.83 to 10.66 eV. Just seven unique cation conformers were found.

The relative conformer populations were calculated at the estimated temperature of the sampled beam, 100 K, and are shown in Figure 9. The Supplementary Material summarizes the calculations and provides detailed information about the zero-point-inclusive conformer energies, locally adiabatic ionization energies, and the output from the M06-2X/aug-cc-pVTZ calculations. Even at the low temperature of 100 K, the hydrogen-bonded structure does not have the largest population, and it comprises only 15% of the total conformer population. The hydrogen-bonded conformer has “tighter” low-frequency modes than the other conformers, and

the resulting effect on the vibrational partition function lowers its population relative to the other conformers. Three conformers with ionization energies near ~10.05 eV together make up 35% of the total population, with the remainder of significantly populated conformers appearing near 10.5-10.7 eV. The experimentally observed ionization energy may be assigned a value of 10.05(±0.05) eV, although we note the presence of small amounts of signal starting around 9.85(±0.05) eV. These features are in good agreement with the results presented in Fig. 8, with the exception that the feature predicted at 9.7 eV is not observed experimentally.

The source of this discrepancy is unclear but may be tentatively attributed to three factors. First, the hydrogen-bonded conformer likely has poorer Franck-Condon overlap than the other conformers, and conformer-dependent Franck-Condon factors were not included in the present analysis. This possibility is supported by the significant relaxation of the cation for the hydrogen-bonded conformer relative to the other conformers. The difference between the calculated vertical and adiabatic ionization energies is 1.6 eV for the hydrogen-bonded conformer, while this difference is only 1.2 eV for the conformers with adiabatic ionization energies near 10.05 eV. Second, the temperature of the beam is not known precisely, and the relative importance of the hydrogen-bonded conformer decreases with increasing temperature. At 250 K, for example, the population of this conformer is only 4%. Third, uncertainties in the calculated populations in the beam are likely even more significant than the uncertainties estimated above due to the unknown temperature of the molecular beam.

Based on this conformer analysis, we may predict the observed ionization energy to have an onset at ~9.8 eV, with pronounced features around 10.0 eV and perhaps again at 10.5 eV. And indeed, the experimentally observed onsets near 9.85 and 10.0 eV (see Fig. 8) match the predicted ones. Based on this analysis we assign m/z = 92.011 u to be the $HOOCH_2OCHO$

intermediate. Further evidence, in the form of its specific fragmentation pattern, is provided in the following paragraphs.

The keto-hydroperoxide can undergo several fragmentation reactions that can lead to further signals in the mass spectrum. To track these fragments we calculated the appearance energy (AE) of different possible fragments and compared them to the PIE curves of the respective masses. From this investigation, signals of *m/z* = 91.003 u ($C_2H_3O_4$), 64.016 u (CH_4O_3) and 59.013 u ($C_2H_3O_2$) were clearly identified as fragments from the keto-hydroperoxide. Their respective PIE curves are plotted in Fig. 8 together with their calculated AEs. It can be clearly seen that the experimentally determined onsets of these curves are in good agreement with the calculated values.

The fragment assigned to *m/z* = 91.003 u is formed through an H-atom loss after the ionization process. In principle, there are 3 different H-atom positions available for fragmentation. The calculated AE = 10.60 eV for the loss of one of the C-bonded H-atoms, forming $HOOCH_2O\dot{C}O^+$, agrees best with the experimental observation of 10.60(±0.05) eV. The fragment with the mass-to-charge ratio of *m/z* = 59.013 u can be assigned to the loss of the HOO-group forming $\dot{C}H_2OCHO^+$. The calculated appearance energy of 10.92 eV is slightly above the observed onset of the PIE curve [10.8(±0.05) eV] but still within the combined experimental and theoretical uncertainties. All calculated ionization energies of *m/z* = 59.013 u species were far off from the experimental observed value (see Table 1). From this observation, we concluded the elimination of $HO\dot{O}$ as a fragment from the keto-hydroperoxide ion as the only consequential possibility.

The signal identification of *m/z* = 64.016 u, which can be assigned to the elemental composition of CH_4O_3, is more difficult. The observation of a strong signal on the respective mass was already reported by Wang *et al.*[24] They assumed this signal to be hydroxymethyl hydroperoxide ($HOCH_2O_2H$, HMHP) or trihydroxymethane [$CH(OH)_3$] and their observed onset of the measured PIE curve is in good agreement with ours [10.15(±0.05) eV]. However, their calculated adiabatic IEs were in the range from 9.77-9.94 eV for HMHP as well as about 11 eV for trihydroxymethane, which are in good agreement with our calculations (see Table 1), but do not comply with the experimental observations. The simplest explanation for the signal on mass 64.016 u would be a CO loss from the formate group of the keto-hydroperoxide HPMF due to fragmentation ($HOOCH_2OCHO^+ \rightarrow HOOCH_2OH^+ + CO$), a typical dissociative reaction of a formate ester.

This dissociation involves an H-atom transfer and a 3-center transition state. This process therefore has two reaction thresholds, one associated with the energy of the saddle point of the 3-center transition state and the other associated with the channel energy of $HOOCH_2OH^+ + CO$. In principle, the appearance of fragmentation may occur at either threshold, or at some intermediate value, where the two thresholds represent the limits where reactive tunneling through the barrier is slow or fast relative to the experimental timescale.

To aid in the assignment of $HOOCH_2OH^+$ as a fragment of $HOOCH_2OCHO^+$, we considered the reference system methylformate [$HC(O)OCH_3^+$], which has the same structural motif and whose fragmentation appearance energies are well known.[81, 86] For methylformate, the experimental appearance energy of CH_3OH^+ is 11.47(± 0.05) eV,[81] which is in closer agreement with the calculated fragmentation channel energy for $CH_3OCHO \rightarrow CH_3OH^+ + CO$ (11.32 eV)

than the calculated 3-center saddle point energy (12.72 eV). Both calculated values were obtained at the ~QCISD(T)/CBS level of theory and include zero point corrections.

Based on this analysis, we anticipate the appearance energy for fragmentation of the hydroperoxymethyl formate cation to $HOOCH_2OH^+$ + CO to be associated with its calculated fragmentation channel energy (10.07 eV) and not its calculated saddle point energy (12.01 eV). In addition to the ±0.05 eV uncertainty assigned to the QCISD(T)/CBS method, the present fragmentation energies have an additional uncertainty of +0.1 eV due to the presence of multiple populated conformers of $HOOCH_2OCHO$, as discussed above.

The experimentally observed appearance energy of 10.15(±0.05) eV for *m/z* = 64.013 u is about the same value (0.08 eV) higher than the calculated product channel energy than it was found for methyl formate (0.15 eV). Based on this discussion we assume *m/z* = 64.013 u to be a fragment from *m/z* = 92.011 u (-CO).

To summarize, the keto-hydroperoxide HPMF has been detected in the low-temperature oxidation processes for DME, and it was identified based on its ionization threshold and its typical fragmentation pattern. Also, our findings indicate that the usual strategy of considering only the lowest-energy conformer might lead to a significantly different prediction for the observable ionization threshold and thus potentially to erroneous isomeric assignments. In Sections 3.3 and 3.4 we provide further evidence for the presence of the keto-hydroperoxide HPMF in the form of intermediates which potentially are formed via dehydrogenation and/or decomposition of HPMF.

3.3. Detection of Formic Acid Anhydride HC(O)OC(O)H at m/z = 74.000 u

As shown by Andersen and Carter,[10] dehydration of HPMF can lead to formic acid anhydride HC(O)OC(O)H (FAA) in a one-step reaction:

$$HOOCH_2OCHO \rightleftarrows HC(O)OC(O)H + H_2O \qquad (R14)$$

In this work, we positively identified FAA at *m/z* = 74.000 u based on a comparison of the experimentally observed ionization threshold with calculated ionization energies. The JSR-sampled PIE curve for this species is shown in Fig. 10. A threshold near 10.65(±0.05) eV is clearly visible and matches the calculated value (10.67 eV). With respect to the calculations, two different conformeric structures had to be considered, the *cis*-configuration with both C=O double bonds having the same orientation and the *trans*-conformer, in which the C=O double bonds are facing opposite directions. The latter one is more stable by about 3 kcal/mol. The adiabatic ionization energies calculated for these conformers are 11.12 and 10.67 eV for the *trans*- and *cis*-conformer, respectively.

It is important to note that our calculations for the appearance energies and ionization energies indicate that FAA is not a fragment of a dissociative ionization process of HPMF (see Table 2). FAA could be directly formed via reaction (R14) or, another possible pathway leading to FAA is the decomposition of the carbonyl-hydroperoxide radical ($\dot{O}CH_2OCHO$),

$$\dot{O}CH_2OCHO \rightleftarrows HC(O)OC(O)H + H, \qquad (R15)$$

which itself is likely to be a product of reaction (R10). However, a more prominent channel for the carbonyl-hydroperoxide decomposition is probably the breaking of the C-O bond leading to CH_2O and $\dot{O}CHO$,

$$\dot{O}CH_2OCHO \rightleftarrows CH_2O + \dot{O}CHO, \qquad (R16)$$

thus providing a reasonable explanation why signal for the formic acid anhydride is rather weak.

In future work, detailed chemical kinetic modeling will be applied to determine the importance of the various conceivable formation pathways.

3.4. Detection of Performic Acid [HC(O)OOH] and Carbonic Acid [HOC(O)OH] at m/z = 62.000 u

Another decomposition product of HPMF is the performic acid [HC(O)OOH] via elimination of H_2 and CO according to reaction (R17):[10]

$$HOOCH_2OCHO \rightleftarrows CH(O)OOH + CO + H_2 \qquad (R17)$$

A doublet signal was observed on mass 62, which could be separated to be CH_2O_3 (*m/z* = 62.000 u) and the ^{18}O isotopologues of $C_2H_2O_2$ species (*m/z* = 62.010 u), which was discussed above as contributions from the 1,3-dioxetane and methyl formate. The separated signals as well as the PIE curve of *m/z* = 62.000 u are depicted in Fig. 11. The signal starts increasing around 10.9(±0.05) eV and thus coincides well with the calculated ionization threshold of performic acid. The lowest-energy conformer of performic acid (labeled (Z,Z) in Ref. [87]) features a 5-center hydrogen bond and has a calculated adiabatic ionization energy of 10.87 eV. The other stable conformer, (E,E), has no hydrogen bond and has a calculated adiabatic ionization energy that is 0.22 eV lower. At 100 K, the populations of the (Z,Z) and (E,E) conformers are 87% and 13%, respectively.

Several other potential pathways for the formation of performic acid were considered in the literature, although more definitive conclusions would require detailed modeling studies. For example, Curran *et al.*[6] have included reaction (R16) in their models and with a subsequent recombination of $\dot{O}CHO$ with OH performic acid could be formed. However, the authors

suggest this recombination to be only a minor channel, as (R16) competes with an internal H-atom transfer via a 5-center transition state and subsequent dissociation

$$\dot{O}CH_2OCHO \rightleftarrows HO\dot{C}HOCHO \rightleftarrows HCO + HC(O)OH. \qquad \text{(R18)}$$

In the modeling studies of Curran *et al.,*[6] the isomerization channel (R18) is determined to be the most important.

We calculated ~QCISD(T)/CBS saddle point energies for (R15), (R16), and R(18) of >35, 19.4, and 12.4 kcal/mol, respectively, where the threshold for (R15) was estimated from partially constrained optimizations. (R18) was found to lead directly to HCO + HC(O)OH products. This finding, as well as the reactive nature of $\dot{O}CHO$, suggests that decomposition of $\dot{O}CH_2OCHO$ is not a major formation pathway of performic acid.

The O_2 + $\dot{C}H_2OCH_2OOH$ reaction leads to $\dot{O}OCH_2OCH_2OOH$ (R7), which is thought to undergo an internal H-atom transfer (R8). The resulting $HOOCH_2O\dot{C}HOOH$ species is typically found to be unstable (or metastable or very weakly bound). The H-atom transfer is instead assumed to form OH and HPMF directly (R9), where the loss of the OH radical can be thought of as arising from a *β*-scission of the transient $HOOCH_2O\dot{C}HOOH$ species. However, we note that there is an additional possible *β*-scission pathway of $HOOCH_2O\dot{C}HOOH$, which for the present system leads to the formation of performic acid, *i.e.,*

$$HOOCH_2O\dot{C}HOOH \rightleftarrows HOO\dot{C}H_2 + HC(O)OOH \qquad \text{(R19)}$$

The potential energy surface associated with (R7) was studied using the M06-2X/aug-cc-pVTZ and ~QCISD(T)/CBS methods, as summarized in Table 3. The adduct $\dot{O}OCH_2OCH_2OOH$ can

undergo H-atom transfer via either a 4- or 6-center transition state, with energies of 7.4 and -12 kcal/mol, respectively, relative to the energy of the entrance channel (O_2 + $\dot{C}H_2OCH_2OOH$). Intrinsic reaction coordinate calculations using the M06-2X/aug-cc-pVTZ method led directly to the OH + $HOOCH_2OCHO$ products, supporting the inclusion of (R9) in detailed models. This is in agreement with detailed chemical kinetic studies of the O_2 + QOOH reaction for other fuels.[50-52, 88]

While (R9) is the dominant pathway, (R19) may be a very minor channel. We were able to find the metastable species $HOOCH_2O\dot{C}HOOH$ at the M06-2X/aug-cc-pVTZ level of theory. Note that this structure is not bound at the B3LYP/aug-cc-pVTZ level of theory. This metastable species is connected to the (R19) products via a saddle point with an energy below that of the reactants (-8 kcal/mol). We estimate this channel to be ~1000x slower than OH loss, which is in fair agreement with the observed signal for these products.

At higher photon energies, contributions from the carbonic acid HOC(O)OH became visible in the PIE curve. The observable onset at 11.27(±0.05) eV is in good agreement with our calculated one at 11.29 eV (see Fig. 12 and Table 1). The appearance of carbonic acid might be explained by a decomposition mechanism which was postulated by Korcek and coworkers.[89-93] This mechanism involves the decomposition of the keto-hydroperoxide via a cyclic intermediate forming an acid and another carbonyl species.[94] In the case of DME two decomposition pathways are conceivable (depicted in Fig. 1) leading to two formic acid molecules or formaldehyde and carbonic acid, respectively. There are several reaction pathways in the low-temperature oxidation of DME forming formic acid and formaldehyde.[6] So, their detection does not allow reliable conclusions of the involvement of the postulated mechanism of Korcek and coworkers in the DME oxidation. However, the appearance of carbonic acid seems to be

justifiable by the Korcek mechanism and its detection might be regarded as experimental evidence. Nevertheless, it should be kept in mind that identification and separation of isomeric species, in this case performic and carbonic acid, can be challenging when the isomers' respective photoionization efficiency curves are unknown.[66, 69, 76]

4. Conclusions

In summary, this paper provides experimental confirmation by detecting and assigning previously unidentified structures formed in the generally accepted oxidation scheme of dimethyl ether at low temperatures. The hydroperoxymethyl formate $HOOCH_2OCHO$ which is expected to be an important intermediate for chain-branching in the low-temperature combustion of dimethyl ether was experimentally detected by mass spectrometry after molecular-beam sampling from a jet-stirred reactor. The experiment employs tunable synchrotron-generated vacuum-ultraviolet radiation and the identification of these species was made possible by a comparison of experimentally observed and calculated ionization and fragment appearance energies. We have shown that the photoionization efficiency curves have to be interpreted with caution due to the influence of different conformeric structures contributing to the observed ionization thresholds. The detection of carbonic acid [HOC(O)OH] may provide experimental evidence for the decomposition of the keto-hydroperoxide according to the mechanism proposed by Korcek and coworkers.

Because mass spectrometry allows the detection of virtually all species simultaneously, additional intermediate species such as performic acid [HC(O)OOH], formic acid anhydride [HC(O)O(O)CH], 1,3-dioxetane (*cycl.*-CH_2-O-CH_2-O-), and methyl hydroperoxide (CH_3OOH) were also successfully identified.

In future work, attempts will be made to quantify the identified species. Once reliable photoionization cross sections of the detected species become available, absolute mole fractions will be accessible for different temperature and flow conditions. Such data will then provide validation targets for the development of chemical models and will ultimately help to identify the important low-temperature oxidation pathways.

Supplementary Information

Details of the theoretical calculations carried out for the neutral and cation conformers from Fig. 9 are summarized in the Supplementary Information. Zero-point-inclusive conformer energies, locally adiabatic ionization energies, and the output from the M06-2X/aug-cc-pVTY calculations are provided. This material is available free of charge via the internet at http://pubs.acs.org.

Acknowledgements:

This material is based upon work supported by the U.S. Department of Energy, Office of Science, Office of Basic Energy Sciences. The work was initiated by the Combustion Energy Frontier Research Center, an Energy Frontier Research Center funded by the U.S. Department of Energy, Office of Basic Energy Sciences under Award Number DE-SC0001198. DMPV and SRL are supported by the Department of Energy Gas Phase Chemical Physics Program at Lawrence Berkeley National Laboratory, under contract DEAC02-05CH11231. DMPV is particularly grateful to the Alexander von Humboldt Foundation for a Feodor Lynen fellowship and she greatly acknowledges the technical support by James Breen, Erik Granlund and William Thur during the designing process and the fabrication of the JSR system. KM and KKH are

grateful for partial support by DFG within the large-scale research structure SFB 686, TP B3. PD has received funding from the European Research Council under the European Community's Seventh Framework Programme (FP7/2007-2013) / ERC grant agreement n° 291049 − 2G-CSafe. Researchers at the Clean Combustion Research Center acknowledge funding from King Abdullah University of Science and Technology. The Advanced Light Source is supported by the Director, Office of Science, Office of Basic Energy Sciences, of the U.S. Department of Energy under Contract No. DEAC02-05CH11231. Sandia is a multi-program laboratory operated by Sandia Corporation, a Lockheed Martin Company, for the National Nuclear Security Administration under contract DE-AC04-94-AL85000.

Disclaimer:

This document was prepared as an account of work sponsored by the United States Government. While this document is believed to contain correct information, neither the United States Government nor any agency thereof, nor the Regents of the University of California, nor any of their employees, makes any warranty, express or implied, or assumes any legal responsibility for the accuracy, completeness, or usefulness of any information, apparatus, product, or process disclosed, or represents that its use would not infringe privately owned rights. Reference herein to any specific commercial product, process, or service by its trade name, trademark, manufacturer, or otherwise, does not necessarily constitute or imply its endorsement, recommendation, or favoring by the United States Government or any agency thereof, or the Regents of the University of California. The views and opinions of authors expressed herein do not necessarily state or reflect those of the United States Government or any agency thereof or the Regents of the University of California.

References

1. Dagaut, P.; Boettner, J.-C.; Cathonnet, M. Chemical kinetic study of dimethylether oxidation in a jet stirred reactor from 1 to 10 atm: Experiments and kinetic modeling. *Proc. Combust. Inst.* **1996,** *26,* 627-632.
2. Pfahl, U.; Fieweger, K.; Adomeit, G. Self-ignition of Diesel-relevant hydrocarbon-air mixtures under engine conditions. *Proc. Combust. Inst.* **1996,** *26,* 781-789.
3. Curran, H. J.; Pitz, W. J.; Westbrook, C. K.; Dagaut, P.; Boettner, J. C.; Cathonnet, M. A wide range modeling study of dimethyl ether oxidation. *Int. J. Chem. Kin.* **1998,** *30,* 229-241.
4. Dagaut, P.; Daly, C.; Simmie, J. M.; Cathonnet, M. The oxidation and ignition of dimethylether from low to high temperature (500-1600 K): Experiments and kinetic modeling. *Proc. Combust. Inst.* **1998,** *27,* 361-369.
5. Yamada, T.; Bozzelli, J. W.; Lay, T. H. Comparisons of CBS-q and G2 calculations on thermodynamic properties, transition states, and kinetics of dimethyl-ether + O2 reaction system. *Int. J. Chem. Kin.* **2000,** *32,* 435-452.
6. Curran, H. J.; Fischer, S. L.; Dryer, F. L. The reaction kinetics of dimethyl ether. II: Low-temperature oxidation in flow reactors. *Int. J. Chem. Kin.* **2000,** *32,* 741-759.
7. Liu, I.; Cant, N. W.; Bromly, J. H.; Barnes, F. J.; Nelson, P. F.; Haynes, B. S. Formate species in the low-temperature oxidation of dimethyl ether. *Chemosphere* **2001,** *42,* 583-589.
8. Dagaut, P.; Luche, J.; Cathonnet, M. The low temperature oxidation of DME and mutual sensitization of the oxidation of DME and nitric oxide: Experimental and detailed kinetic modeling. *Combust. Sci. Tech.* **2001,** *165,* 61-84.

9. Andersen, A.; Carter, E. A. A hybrid density functional theory study of the low-temperature dimethyl ether combustion pathways. I: Chain-propagation. *Isr. J. Chem.* **2002,** *42,* 245-260.

10. Andersen, A.; Carter, E. A. Hybrid density functional theory predictions of low-temperature dimethyl ether combustion pathways. II. Chain-branching energetics and possible role of the Criegee intermediate. *J. Phys. Chem. A* **2003,** *107,* 9463-9478.

11. Yamada, H.; Suzaki, K.; Sakanashi, H.; Choi, N.; Tezaki, A. Kinetic measurements in homogeneous charge compression of dimethyl ether: role of intermediate formaldehyde controlling chain branching in the low-temperature oxidation mechanism. *Combust. Flame* **2005,** *140,* 24-33.

12. Rosado-Reyes, C. M.; Francisco, J. S.; Szente, J. J.; Maricq, M. M.; Østergaard, L. F. Dimethyl ether oxidation at elevated temperatures (295-600 K). *J. Phys. Chem. A* **2005,** *109,* 10940-10953.

13. Suzaki, K.; Kanno, N.; Tonokura, K.; Koshi, M.; Tsuchiya, K.; Tezaki, A. Formation of HO_2 and OH in photolytically initiated oxidation of dimethyl ether. *Chem. Phys. Lett.* **2006,** *425,* 179-184.

14. Andersen, A.; Carter, E. A. Insight into selected reactions in low-temperature dimethyl ether combustion from Born-Oppenheimer molecular dynamics. *J. Phys. Chem. A* **2006,** *110,* 1393-1407.

15. Suzaki, K.; Tsuchiya, K.; Koshi, M.; Tezaki, A. Analysis of HO_2 and OH formation mechanisms using FM and UV spectroscopy in dimethyl ether oxidation. *J. Phys. Chem. A* **2007,** *111,* 3776-3788.

16. Zhao, Z.; Chaos, M.; Kazakov, A.; Dryer, F. L. Thermal decomposition reaction and a comprehensive kinetic model of dimethyl ether. *Int. J. Chem. Kin.* **2008,** *40,* 1-18.

17. Andersen, A.; Carter, E. A. First-principles-derived kinetics of the reactions involved in the low-temperature dimethyl ether oxidation. *Mol. Phys.* **2008,** *106,* 367-396.

18. Guo, H.; Sun, W.; Haas, F. M.; Farouk, T.; Dryer, F. L.; Ju, Y. Measurements of H_2O_2 in low temperature dimethyl ether oxidation. *Proc. Combust. Inst.* **2013,** *34,* 573-581.

19. Carr, S. A.; Still, T. J.; Blitz, M. A.; Eskola, A. J.; Pilling, M. J.; Seakins, P. W.; Shannon, R. J.; Wang, B.; Robertson, S. H. Experimental and theoretical study of the kinetics and mechanism of the reaction of OH radicals with dimethyl ether. *J. Phys. Chem. A* **2013,** *117,* 11142-11154.

20. Zhang, K. W.; Moshammer, K.; Oßwald, P.; Kohse-Höinghaus, K. Experimental investigation of partially premixed, highly-diluted dimethyl ether flames at low temperatures. *Proc. Combust. Inst.* **2013,** *34,* 763-770.

21. Herrmann, F.; Oßwald, P.; Kohse-Höinghaus, K. Mass spectrometric investigation of the low-temperature dimethyl ether oxidation in an atmospheric pressure laminar flow reactor. *Proc. Combust. Inst.* **2013,** *34,* 771-778.

22. Herrmann, F.; Jochim, B.; Oßwald, P.; Cai, L.; Pitsch, H.; Kohse-Höinghaus, K. Experimental and numerical low-temperature oxidation study of ethanol and dimethyl ether. *Combust. Flame* **2014,** *161,* 384-397.

23. Eskola, A. J.; Carr, S. A.; Shannon, R. J.; Wang, B.; Blitz, M. A.; Pilling, M. J.; Seakins, P. W.; Robertson, S. H. Analysis of the kinetics and yiels of OH radical production from the CH_3OCH_2+O_2 reaction in the temperature range 195-650 K: An experimental and theoretical study. *J. Phys. Chem. A* **2014,** *118,* 6773-6788.

24. Wang, Z.; Zhang, X.; Xing, L.; Zhang, L.; Herrmann, F.; Moshammer, K.; Qi, F.; Kohse-Höinghaus, K. Experimental and kinetic modeling study of the low- and intermediate-temperature oxidation of dimethyl ether. *Combust. Flame* **2014,** http://dx.doi.org/10.1016/j.combustflame.2014.10.003.

25. Kurimoto, N.; Brumfield, B.; Yang, X.; Wada, T.; Diévart, P.; Wysocki, G.; Ju, Y. Quantitative measurements of HO_2/H_2O_2 and intermediate species in low and intermediate temperature oxidation of dimethyl ether. *Proc. Combust. Inst.* **2015,** *35,* 457-464.

26. Imtenan, S.; Varman, M.; Masjuki, H. H.; Kalam, M. A.; Sajjad, H.; Arbab, M. I.; Fattah, I. M. R. Impact of low temperature combustion attaining strategies on diesel engine emissions for diesel and biodiesels: A review. *Energ. Convers. Manage.* **2014,** *80,* 329-356.

27. Saxena, S.; Bedoya, I. D. Fundamental phenomena affecting low temperature combustion and HCCI engines, high load limits and strategies for extending these limits. *Prog. Energy Combust. Sci.* **2013,** *39,* 457-488.

28. Arcoumanis, C.; Bae, C.; Crookes, R.; Kinoshita, E. The potential of dimethyl ether (DME) as an alternative fuel for compression-ignition engines: A review. *Fuel* **2008,** *87,* 1014-1030.

29. Semelsberger, T. A.; Borup, R. L.; Greene, H. L. Dimethyl ether (DME) as an alternative fuel. *J. Power Sources* **2006,** *156,* 497-511.

30. Azizi, Z.; Rezaeimanesh, M.; Tohidian, T.; Rahimpour, M. R. Dimethyl ether: A review of technologies and production challenges. *Chem. Eng. Process.* **2014,** *82,* 150-172.

31. Kaiser, E. W.; Wallington, T. J.; Hurley, M. D.; Platz, J.; Curran, H. J.; Pitz, W. J.; Westbrook, C. K. Experimental and modeling study of premixed atmospheric-pressure dimethyl ether-air flames. *J. Phys. Chem. A* **2000,** *104,* 8194-8206.

32. Hidaka, Y.; Sato, K.; Yamane, M. High-temperature pyrolysis of dimethyl ether in shock waves. *Combust. Flame* **2000,** *123,* 1-22.

33. Fischer, S. L.; Dryer, F. L.; Curran, H. J. The reaction kinetics of dimethyl ether. I: High-temperature pyrolysis and oxidation in flow reactors. *Int. J. Chem. Kin.* **2000,** *32,* 713-740.

34. Daly, C. A.; Simmie, J. M.; Wurmel, J.; Djebaili, N.; Paillard, C. Burning velocities of dimethyl ether and air. *Combust. Flame* **2001,** *125,* 1329-1340.

35. Zhao, Z.; Kazakov, A.; Dryer, F. L. Measurements of dimethyl ether/air mixture burning velocities by using particle image velocimetry. *Combust. Flame* **2004,** *139,* 52-60.

36. Qin, X.; Ju, Y. G. Measurements of burning velocities of dimethyl ether and air premixed flames at elevated pressures. *Proc. Combust. Inst.* **2005,** *30,* 233-240.

37. Cool, T. A.; Wang, J.; Hansen, N.; Westmoreland, P. R.; Dryer, F. L.; Zhao, Z.; Kazakov, A.; Kasper, T.; Kohse-Höinghaus, K. Photoionization mass spectrometry and modeling studies of the chemistry of fuel-rich dimethyl ether flames. *Proc. Combust. Inst.* **2007,** *31,* 285-293.

38. Wang, J.; Chaos, M.; Yang, B.; Cool, T. A.; Dryer, F. L.; Kasper, T.; Hansen, N.; Oßwald, P.; Kohse-Höinghaus, K.; Westmoreland, P. R. Composition of reaction intermediates for stoichiometric and fuel-rich dimethyl ether flames: flame-sampling mass spectrometry and modeling studies. *Phys. Chem. Chem. Phys.* **2009,** *11,* 1328-1339.

39. Cook, R. D.; Davidson, D. F.; Hanson, R. K. High-temperature shock tube measurements of dimethyl ether decomposition and the reaction of dimethyl ether with OH. *J. Phys. Chem. A* **2009,** *113,* 9974-9980.

40. Wang, Y. L.; Holley, A. T.; Ji, C.; Egolfopoulos, F. N.; Tsotsis, T. T.; Curran, H. J. Propagation and extinction of premixed dimethyl-ether/air flames. *Proc. Combust. Inst.* **2009,** *32,* 1035-1042.

41. Chen, Z. Y.; Wei, L. X.; Gu, X. L.; Huang, Z. H.; Yuan, T.; Li, Y. Y.; Tian, Z. Y. Study of low-pressure premixed dimethyl ether/hydrogen/oxygen/argon laminar flames with photoionization mass spectrometry. *Energy Fuels* **2010,** *24,* 1628-1635.

42. Sivaramakrishnan, R.; Michael, J. V.; Wagner, A. F.; Dawes, R.; Jasper, A. W.; Harding, L. B.; Georgievskii, Y.; Klippenstein, S. J. Roaming radicals in the thermal decomposition of dimethyl ether: Experiment and theory. *Combust. Flame* **2011,** *158,* 618-632.

43. Xu, H. J.; Yao, C. D.; Yuan, T.; Zhang, K. W.; Guo, H. J. Measurements and modeling study of intermediates in ethanol and dimethy ether low-pressure premixed flames using synchrotron photoionization. *Combust. Flame* **2011,** *158,* 1673-1681.

44. Chen, Z. Y.; Tang, C. L.; Fu, J.; Jiang, X.; Li, Q. Q.; Wei, L. J.; Huang, Z. H. Experimental and numerical investigation on diluted DME flames: Thermal and chemical kinetic effects on laminar flame speeds. *Fuel* **2012,** *102,* 567-573.

45. Tranter, R. S.; Lynch, P. T.; Yang, X. L. Dissociation of dimethyl ether at high temperatures. *Proc. Combust. Inst.* **2013,** *34,* 591-598.

46. Pyun, S. H.; Ren, W.; Lam, K. Y.; Davidson, D. F.; Hanson, R. K. Shock tube measurements of methane, ethylene and carbon monoxide time-histories in DME pyrolysis. *Combust. Flame* **2013,** *160,* 747-754.

47. Liu, D.; Santner, J.; Togbe, C.; Felsmann, D.; Koppmann, J.; Lackner, A.; Yang, X. L.; Shen, X. B.; Ju, Y. G.; Kohse-Höinghaus, K. Flame structure and kinetic studies of carbon dioxide-diluted dimethyl ether flames at reduced and elevated pressures. *Combust. Flame* **2013,** *160,* 2654-2668.

48. Zheng, X. L.; Lu, T. F.; Law, C. K.; Westbrook, C. K.; Curran, H. J. Experimental and computational study of nonpremixed ignition of dimethyl ether in counterflow. *Proc. Combust. Inst.* **2005,** *30,* 1101-1109.

49. Sehested, J.; Mogelberg, T.; Wallington, T. J.; Kaiser, E. W.; Nielsen, O. J. Dimethyl ether oxidation: Kinetics and mechanism of the CH_3OCH_2+O_2 reaction at 296 K and 0.38-940 Torr total pressure. *J. Phys. Chem.* **1996,** *100,* 17218-17225.

50. Battin-Leclerc, F. Detailed chemical kinetic models for the low-temperature combustion of hydrocarbons with application to gasoline and diesel fuel surrogates. *Prog. Energy Combust. Sci.* **2008,** *34,* 440-498.

51. Zador, J.; Taatjes, C. A.; Fernandes, R. X. Kinetics of elementary reactions in low-temperature autoignition chemistry. *Prog. Energy Combust. Sci.* **2011,** *37,* 371-421.

52. Sarathy, S. M.; Oßwald, P.; Hansen, N.; Kohse-Höinghaus, K. Alcohol combustion chemistry. *Progr. Energy Combust. Sci.* **2014,** *44,* 40-102.

53. Herbinet, O.; Dayma, G. Jet-stirred reactor. In *Cleaner Combustion*, Battin-Leclerc, F.; Simmie, J. M.; Blurock, E., Eds. Springer-Verlag: London, 2013.

54. Bahrini, C.; Herbinet, O.; Glaude, P. A.; Schoemaecker, C.; Fittschen, C.; Battin-Leclerc, F. Quantification of hydrogen peroxide during the low-temperature oxidation of alkanes. *J. Am. Chem. Soc.* **2012,** *134,* 11944-11947.

55. Bahrini, C.; Herbinet, O.; Glaude, P. A.; Schoemaecker, C.; Fittschen, C.; Battin-Leclerc, F. Detection of some stable species during the oxidation of methane by coupling a jet-stirred reactor (JSR) to cw-CRDS. *Chem. Phys. Lett.* **2012,** *534,* 1-7.

56. Bahrini, C.; Morajkar, P.; Schoemaecker, C.; Frottier, O.; Herbinet, O.; Glaude, P. A.; Battin-Leclerc, F.; Fittschen, C. Experimental and modeling study of the oxidation of n-butane in a jet stirred reactor using cw-CRDS measurements. *Phys. Chem. Chem. Phys.* **2013,** *15,* 19686-19698.

57. Djehiche, M.; Le Tan, N. L.; Jain, C.; Dayma, G.; Dagaut, P.; Chauveau, C.; Pillier, L.; Tomas, A. Quantitative measurements of HO_2 and other products of n-butane oxidation (H_2O_2, H_2O, CH_2O, and C_2H_4) at elevated temperatures by direct coupling of a jet-stirred reactor with sampling nozzle and cavity ring-down spectroscopy (cw-CRDS). *J. Am. Chem. Soc.* **2014,** *136,* 16689-16694.

58. Dubreuil, A.; Foucher, F.; Mounaim-Rousselle, C.; Dayma, G.; Dagaut, P. HCCI combustion: effect of NO in EGR. *Proc. Combust. Inst.* **2007,** *31,* 2879-2886.

59. Battin-Leclerc, F.; Herbinet, O.; Glaude, P.-A.; Fournet, R.; Zhou, Z.; Deng, L.; Guo, H.; Xie, M.; Qi, F. Experimental confirmation of the low-temperature oxidation scheme of alkanes. *Angew. Chem. Int. Ed.* **2010,** *49,* 3169-3172.

60. Herbinet, O.; Battin-Leclerc, F.; Bax, S.; Le Gall, H.; Glaude, P. A.; Fournet, R.; Zhou, Z. Y.; Deng, L. L.; Guo, H. J.; Xie, M. F.*, et al.* Detailed product analysis during the low temperature oxidation of n-butane. *Phys. Chem. Chem. Phys.* **2011,** *13,* 296-308.

61. Cord, M.; Husson, B.; Lizardo Huerta, J. C.; Herbinet, O.; Glaude, P. A.; Fournet, R.; Sirjean, B.; Battin-Leclerc, F.; Ruiz-Lopez, M.; Wang, Z. D.*, et al.* Study of the low temperature oxidation of propane. *J. Phys. Chem. A* **2012,** *116,* 12214-12228.

62. Herbinet, O.; Husson, B.; Serinyel, Z.; Cord, M.; Warth, V.; Fournet, R.; Glaude, P. A.; Sirjean, B.; Battin-Leclerc, F.; Wang, Z. D.*, et al.* Experimental and modeling investigation of the low-temperature oxidation of n-heptane. *Combust. Flame* **2012,** *159,* 3455-3471.

63. Battin-Leclerc, F.; Rodriguez, A.; Husson, B.; Herbinet, O.; Glaude, P. A.; Wang, Z. D.; Cheng, Z. J.; Qi, F. Products from the oxidation of linear isomers of hexene. *J. Phys. Chem. A* **2014,** *118,* 673-683.

64. Wang, Z. D.; Herbinet, O.; Cheng, Z. J.; Husson, B.; Fournet, R.; Qi, F.; Battin-Leclerc, F. Experimental investigation of the low temperature oxidation of the five isomers of hexane. *J. Phys. Chem. A* **2014,** *118,* 5573-5594.

65. Battin-Leclerc, F.; Herbinet, O.; Glaude, P. A.; Fournet, R.; Zhou, Z. Y.; Deng, L. L.; Guo, H. J.; Xie, M. F.; Qi, F. New experimental evidences about the formation and consumption of ketohydroperoxides. *Proc. Combust. Inst.* **2011,** *33,* 325-331.

66. Hansen, N.; Cool, T. A.; Westmoreland, P. R.; Kohse-Höinghaus, K. Recent contributions of flame-sampling molecular-beam mass spectrometry to a fundamental understanding of combustion chemistry. *Prog. Energy Combust. Sci.* **2009,** *35,* 168-191.

67. Qi, F. Combustion chemistry probed by synchrotron VUV photoionization mass spectrometry. *Proc. Combust. Inst.* **2013,** *34,* 33-63.

68. Leone, S. R.; Ahmed, M.; Wilson, K. R. Chemical dynamics, molecular energetics, and kinetics at the synchrotron. *Phys. Chem. Chem. Phys.* **2010,** *12,* 6564-6578.

69. Egolfopoulos, F. N.; Hansen, N.; Ju, Y.; Kohse-Höinghaus, K.; Law, C. K.; Qi, F. Advances and challenges in experimental research of combustion chemistry in laminar flames. *Prog. Energy Combust. Sci.* **2014,** *43,* 36-67.

70. Hansen, N.; Braun-Unkhoff, M.; Kathrotia, T.; Lucassen, A.; Yang, B. Understanding the reaction pathways in premixed flames fueled by blends of 1,3-butadiene and n-butanol. *Proc. Combust. Inst.* **2015,** *35,* 771-778.

71. Lucassen, A.; Park, S.; Hansen, N.; Sarathy, S. M. Combustion chemistry of alcohols: Experimental and modeled structure of a premixed 2-methylbutanol flame. *Proc. Combust. Inst.* **2015,** *35,* 813-820.

72. Martin, J. M. L.; Uzan, O. Basis set convergence in second-row compounds. The importance of core polarization functions. *Chem. Phys. Lett.* **1998,** *282,* 16-24.

73. Hansen, N.; Kasper, T.; Klippenstein, S. J.; Westmoreland, P. R.; Law, M. E.; Taatjes, C. A.; Kohse-Höinghaus, K.; Wang, J.; Cool, T. A. Initial steps of aromatic ring formation in a laminar premixed fuel-rich cyclopentene flame. *J. Phys. Chem. A* **2007,** *111,* 4081-4092.

74. Hansen, N.; Klippenstein, S. J.; Miller, J. A.; Wang, J.; Cool, T. A.; Law, M. E.; Westmoreland, P. R.; Kasper, T.; Kohse-Höinghaus, K. Identification of C_5H_x isomers in fuel-rich flames by photoionization mass spectrometry and electronic structure calculations. *J. Phys. Chem. A* **2006,** *110,* 4376-4388.

75. Hansen, N.; Klippenstein, S. J.; Taatjes, C. A.; Miller, J. A.; Wang, J.; Cool, T. A.; Yang, B.; Yang, R.; Wei, L. X.; Huang, C. Q.*, et al.* Identification and chemistry of C_4H_3 and C_4H_5 isomers in fuel-rich flames. *J. Phys. Chem. A* **2006,** *110,* 3670-3678.

76. Hansen, N.; Klippenstein, S. J.; Westmoreland, P. R.; Kasper, T.; Kohse-Höinghaus, K.; Wang, J.; Cool, T. A. A combined ab initio and photoionization mass spectrometric study of polyynes in fuel-rich flames. *Phys. Chem. Chem. Phys.* **2008,** *10,* 366-374.

77. Li, Z. H.; Jasper, A. W.; Truhlar, D. G. Structures, rugged energetic landscapes, and nanothermodynamics of Al_n (2 <= n <= 65) particles. *J. Am. Chem. Soc.* **2007,** *129,* 14899-14910.

78. Zheng, J. J.; Truhlar, D. G. Quantum thermochemistry: Multistructural method with torsional anharmonicity based on a coupled torsional potential. *J. Chem. Theory Comput.* **2013,** *9,* 1356-1367.

79. Krüger, J.; Garcia, G. A.; Felsmann, D.; Moshammer, K.; Lackner, A.; Brockhinke, A.; Nahon, L.; Kohse-Höinghaus, K. Photoelectron-photoion coincidence spectroscopy for multiplexed detection of intermediate species in a flame. *Phys. Chem. Chem. Phys.* **2014,** *16,* 22791-22804.

80. Cool, T. A.; McIlroy, A.; Qi, F.; Westmoreland, P. R.; Poisson, L.; Peterka, D. S.; Ahmed, M. Photoionization mass spectrometer for studies of flame chemistry with a synchrotron light source. *Rev. Sci. Instr.* **2005,** *76*.

81. Lias, S. G., "Ionization Energy Evaluation" in NIST Chemistry WebBook, NIST Standard Reference Database Number 69, Eds. Linstrom, P. J.; Mallard, W. G., National Institute of Standards and Technology, Gaithersburg MD 20899, http://webbook.nist.gov (accessed November 2014).

82. Nguyen, M. T.; Nguyen, T. L.; Ngan, V. T.; Nguyen, H. M. T. Heats of formation of the Criegee formaldehyde oxide and dioxirane. *Chem. Phys. Lett.* **2007,** *448,* 183-188.

83. Hansen, N.; Harper, M. R.; Green, W. H. High-temperature oxidation chemistry of n-butanol - experiments in low-pressure premixed flames and detailed kinetic modeling. *Phys. Chem. Chem. Phys.* **2011,** *13,* 20262-20274.

84. Hansen, N.; Li, W.; Law, M. E.; Kasper, T.; Westmoreland, P. R.; Yang, B.; Cool, T. A.; Lucassen, A. The importance of fuel dissociation and propargyl plus allyl association for the formation of benzene in a fuel-rich 1-hexene flame. *Phys. Chem. Chem. Phys.* **2010,** *12,* 12112-12122.

85. Hansen, N.; Miller, J. A.; Westmoreland, P. R.; Kasper, T.; Kohse-Höinghaus, K.; Wang, J.; Cool, T. A. Isomer-specific combustion chemistry in allene and propyne flames. *Combust. Flame* **2009,** *156,* 2153-2164.

86. Wang, J.; Yang, B.; Cool, T. A.; Hansen, N. Absolute cross-sections for dissociative photoionization of some small esters. *Int. J. Mass Spectrom.* **2010,** *292,* 14-22.

87. Domanskaya, A. V.; Ermilov, A.; Andrijchenko, N.; Khriachtchev, L. The other conformer of peroxyformic acid. *Mol. Phys.* **2010,** *108,* 2369-2375.

88. Goldsmith, C. F.; Green, W. H.; Klippenstein, S. J. Role of O_2 + QOOH in low-temperature ignition of propane. 1. Temperature and pressure dependent rate coefficients. *J. Phys. Chem. A* **2012,** *116,* 3325-3346.

89. Jensen, R. K.; Korcek, S.; Mahoney, L. R.; Zinbo, M. Liquid-phase autooxidation of organic-compounds at elevated-temperatures. 1. Stirred flow reactor technique and analysis of primary products from normal-hexadecane autoxidation at 120-degrees-C 180-degrees-C. *J. Am. Chem. Soc.* **1979,** *101,* 7574-7584.

90. Hamilton, E. J.; Korcek, S.; Mahoney, L. R.; Zinbo, M. Kinetics and mechanism of the autoxidation of pentaerythrityl tetraheptanoate at 180-220 °C. *Int. J. Chem. Kin.* **1980,** *12,* 577-603.

91. Jensen, R. K.; Korcek, S.; Mahoney, L. R.; Zinbo, M. Liquid-phase autooxidation of organic-compounds at elevated-temperatures. 2. Kinetics and mechanisms of the formation of cleavage products in normal-hexadecane autoxidation. *J. Am. Chem. Soc.* **1981,** *103,* 1742-1749.

92. Jensen, R. K.; Zinbo, M.; Korcek, S. HPLC Determination of hydroperoxidic products formed in the autoxidation of normal-hexadecane at elevated-temperatures. *J. Chromatogr. Sci.* **1983,** *21,* 394-397.

93. Jensen, R. K.; Korcek, S.; Zinbo, M.; Johnson, M. D. Initiation in hydrocarbon autoxidation at elevated-temperatures. *Int. J. Chem. Kin.* **1990,** *22,* 1095-1107.

94. Jalan, A.; Alecu, I. M.; Meana-Paneda, R.; Aguilera-Iparraguirre, J.; Yang, K. R.; Merchant, S. S.; Truhlar, D. G.; Green, W. H. New pathways for formation of acids and carbonyl products in low-temperature oxidation: The Korcek decomposition of gamma-ketohydroperoxides. *J. Am. Chem. Soc.* **2013,** *135,* 11100-11114.

Tables

Table 1: Calculated adiabatic ionization energies (eV)

m/*z*	Species	Theory I[a]	Theory II[b]
48	CH_3OOH	9.77	9.83
	$HOCH_2OH$	11.00	11.10
59	CH_2OCHO	7.93	7.78
	CH_2CHOO	10.18	9.79
60	$HC(O)OCH_3$	10.81	10.86
	CH_2CHOOH	9.07	9.19
	HOCHCHOH	8.27	8.41
	oxiran-2-ol	8.83	8.87
	3-CH_3-dioxirane	10.31	10.30
	cycl.-CH_2OOCH_2-	9.35	9.37
	cycl.-CH_2OCH_2O-	10.00	10.08
62	HC(O)OOH	10.89	10.87
	HOC(O)OH	11.25	11.29
	CH_3CH_2OOH	9.54	9.61
	CH_3OCH_2OH	9.81	10.05
	CH_3OOCH_3	9.16	9.21
	$HOCH_3CH_3OH$	9.55	9.69
64	CH_3OOOH	9.90	9.92
	$HOOCH_2OH$	9.77	9.83
	$HC(OH)_3$	10.94	10.98
74	HC(O)O(O)CH	11.13	11.12[c]
78	CH_3OCH_2OOH	9.59	9.60[c]
	CH_3OOCH_2OH	9.26	
91	$OOCH_2OCHO$	10.49	
	HOOCHOCHO	6.88	
	$HOOCH_2OCO$	6.52	
92	$OCHOCH_2OOH$	~10[c]	~10[c]
	cycl.-$CH_2OOCH(OH)O$-	9.59	9.65

[a]M06-2X/aug-cc-pVTZ
[b]~QCISD(T)/CBS//M06-2X/aug-cc-pVTZ
[c]See text for a detailed conformational analysis.

Table 2: Fragmentation channel energies (eV)

m	Parent	*m*/*z*	Fragment Ion	Theory I[a]	Theory II[b]
92	$HOOCH_2OCHO$	59	CH_2OCHO^+	11.04	10.92
		60	CH_3OCHO^+	11.75	11.83
		64	$HOOCH_2OH^+$	10.13	10.07
		74	$OCHOCHO^+$	8.41	8.29
		91	$OOCH_2OCHO^+$	14.29	
		91	$HOOCHOCHO^+$	11.12	11.09
		91	$HOOCH_2OCO^+$	10.73	10.60

[a]M06-2X/aug-cc-pVTZ

[b]~QCISD(T)/CBS//M06-2X/aug-cc-pVTZ

Table 3: Zero-point inclusive O_2 + QOOH potential energy surface (kcal/mol)

Species	Label	Theory I[a]	Theory II[b]
$O_2 + CH_2OCH_2OOH$	R	0.0	0.0
$OOCH_2OCH_2OOH$	W1	–34.1	
$HOOCH_2OCHOOH$	W2	–22.7	–22.1
$OH + OCHOCH_2OOH$	P1	–73.1	
$OCHOOH + HOOCH_2$	P2	–25.2	
$OCHOOH + HO + OCH_2$	P2'	–57.3	
4-center H-transfer	$[W1 = P1]^{\ddagger}$	8.6	7.4
6-center H-transfer	$[W1 = P1]^{\ddagger}$	–11.0	–12.0
O–O β-scission	$[W2 = P1]^{\ddagger}$	–23.3[c]	
C–O β-scission	$[W2 = P2]^{\ddagger}$	–8.0	–9.7

[a]M06-2X/aug-cc-pVTZ

[b]~QCISD(T)/CBS//M06-2X/aug-cc-pVTZ

[c]W2 is bound by 0.94 kcal/mol before the zero point correction.

Figures

Figure 1:

Schematic of the dimethyl ether oxidation steps at low temperatures. See text for more details; the reactions are labeled in accordance with the numbering in the main text. Molecular structures that are discussed in the manuscript are labeled with their mass-to-charge ratio *m/z* (for mass spectrometric detection) and their names.

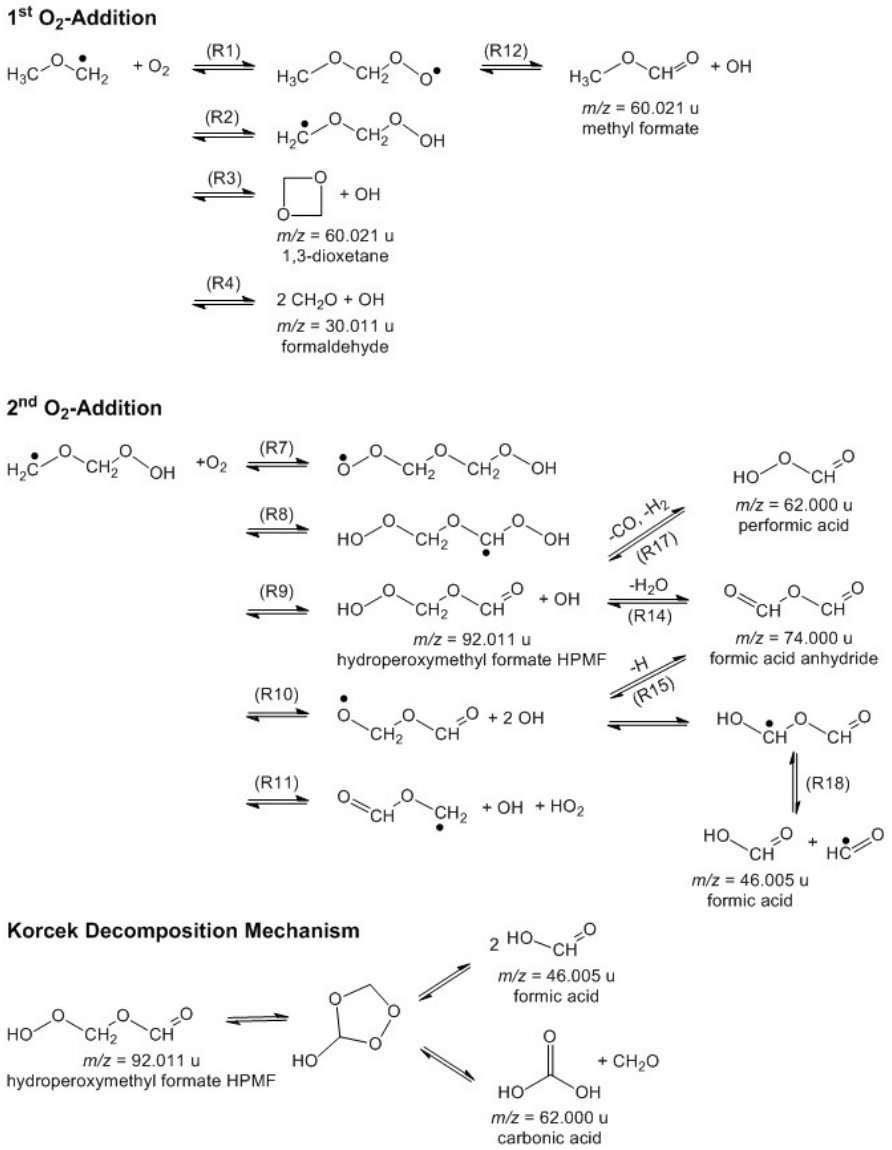

Figure 2:

Schematic representation of the experimental set-up. Shown in the figure is the jet-stirred reactor that is located within an oven, all surrounded by a water-cooled stainless steel chamber. Molecules are sampled from the reactor through a quartz probe, ionized via single-photon ionization with vacuum-ultraviolet photons and the respective ions are mass-selected using a reflectron time-of-flight mass spectrometer.

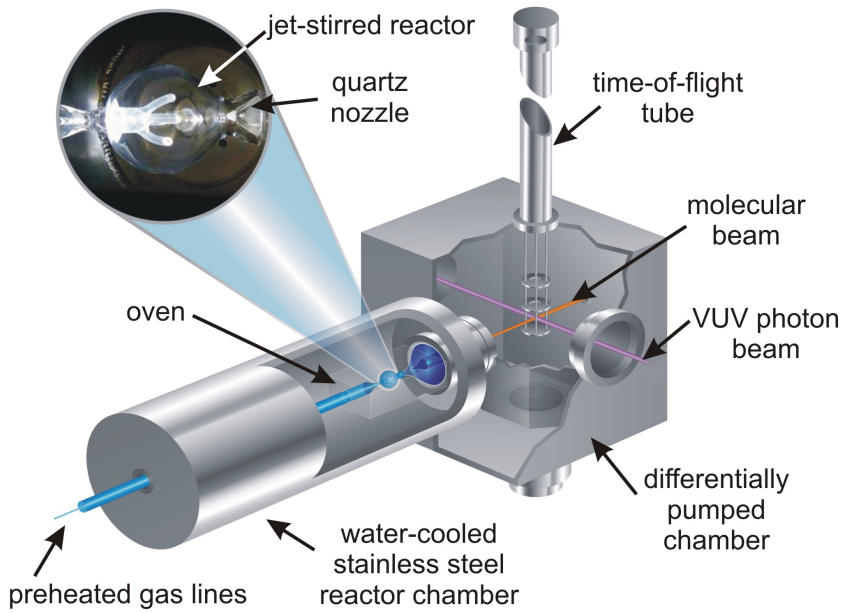

Figure 3:

Overview mass spectrum in the range of *m/z* = 25-100 u recorded at 11.2 eV. Peaks discussed in this manuscript are labeled with their corresponding elemental compositions.

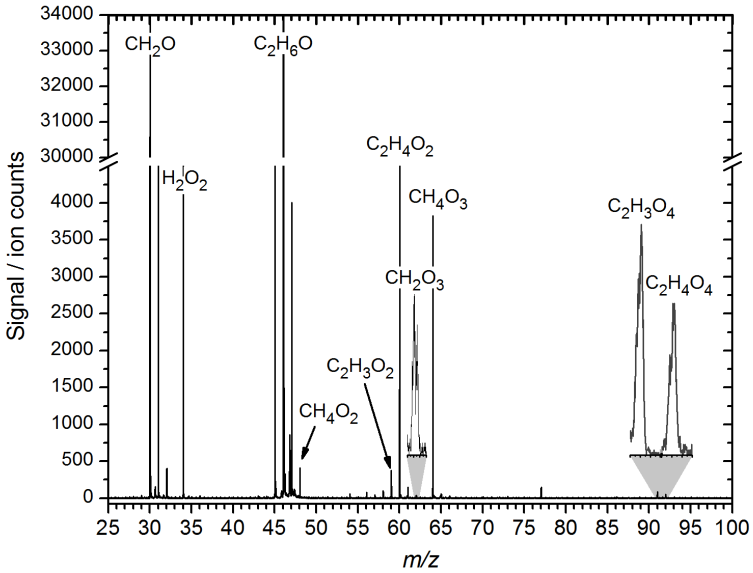

Figure 4:

JSR-sampled photoionization efficiency curves of *m/z* = 30.011 u and 34.005 u. Based on the observed ionization thresholds and known ionization energies, the signal can easily be assigned to originate from formaldehyde and hydrogenperoxide.

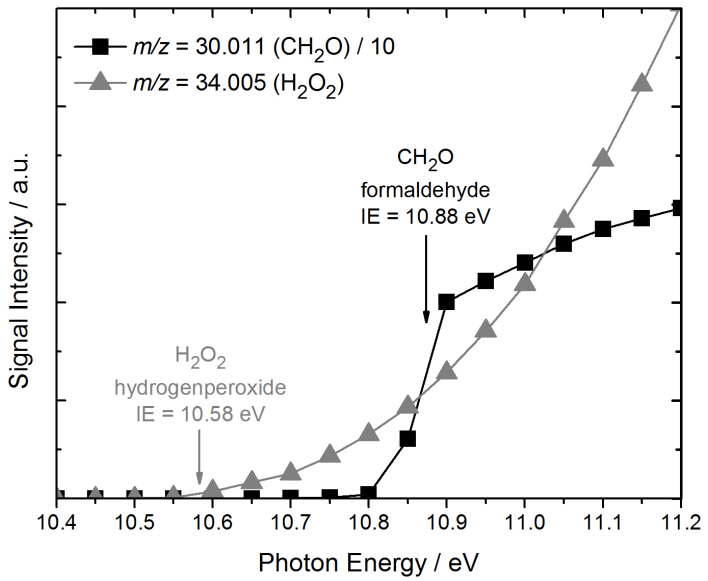

Figure 5:

(a) JSR-sampled, high-resolution mass spectrum at *m/z* = 46 u recorded at 11.7 eV. Two peaks are clearly visible which can be assigned to CH_2O_2 and C_2H_6O. The C_2H_6O can be identified as the fuel (DME). (b) The photoionization efficiency curve allows for the identification of CH_2O_2 as formic acid HC(O)OH.

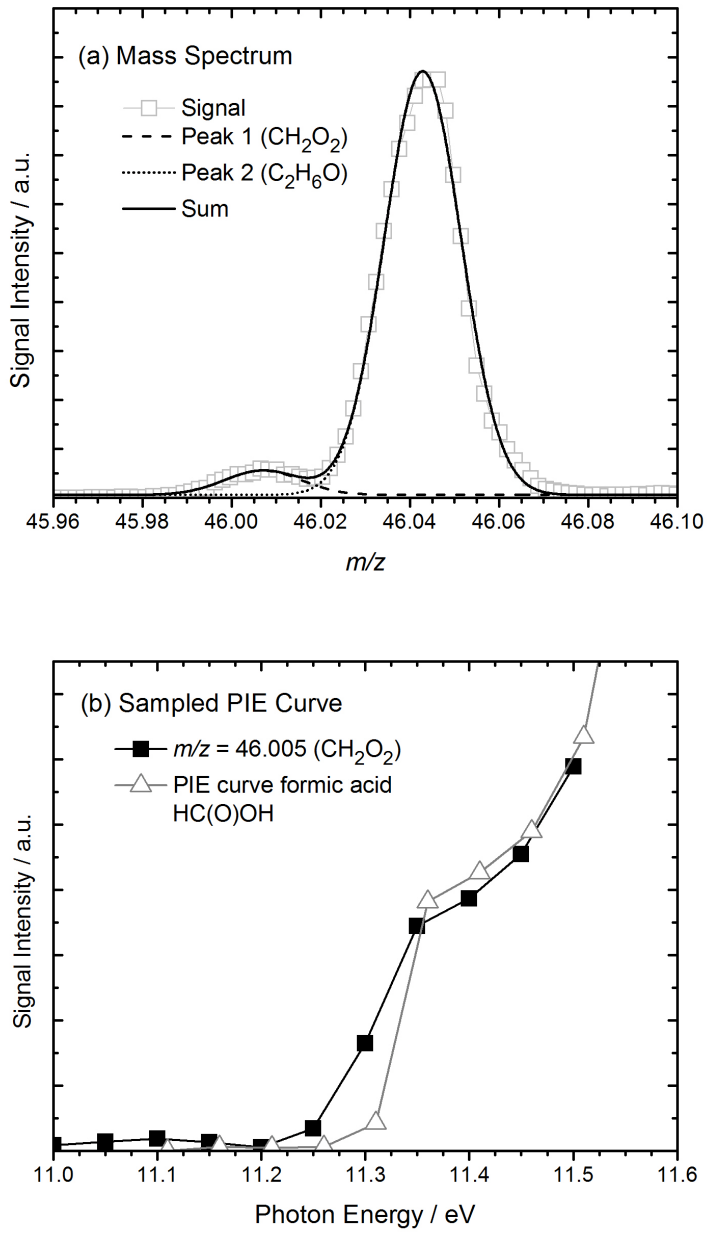

Figure 6:

(a) JSR-sampled, high-resolution mass spectrum at *m/z* = 48 u taken at 11.2 eV. Two peaks are clearly visible which can be assigned to CH_4O_2 and $C_2H_6{}^{18}O$. The $C_2H_6{}^{18}O$ is identified as the ^{18}O isotopomer of the fuel (DME), (b) The observed ionization threshold near 9.85(±0.05) eV for CH_4O_2 allows for the identification of CH_4O_2 as methyl hydroperoxide (calc. IE = 9.83 eV).

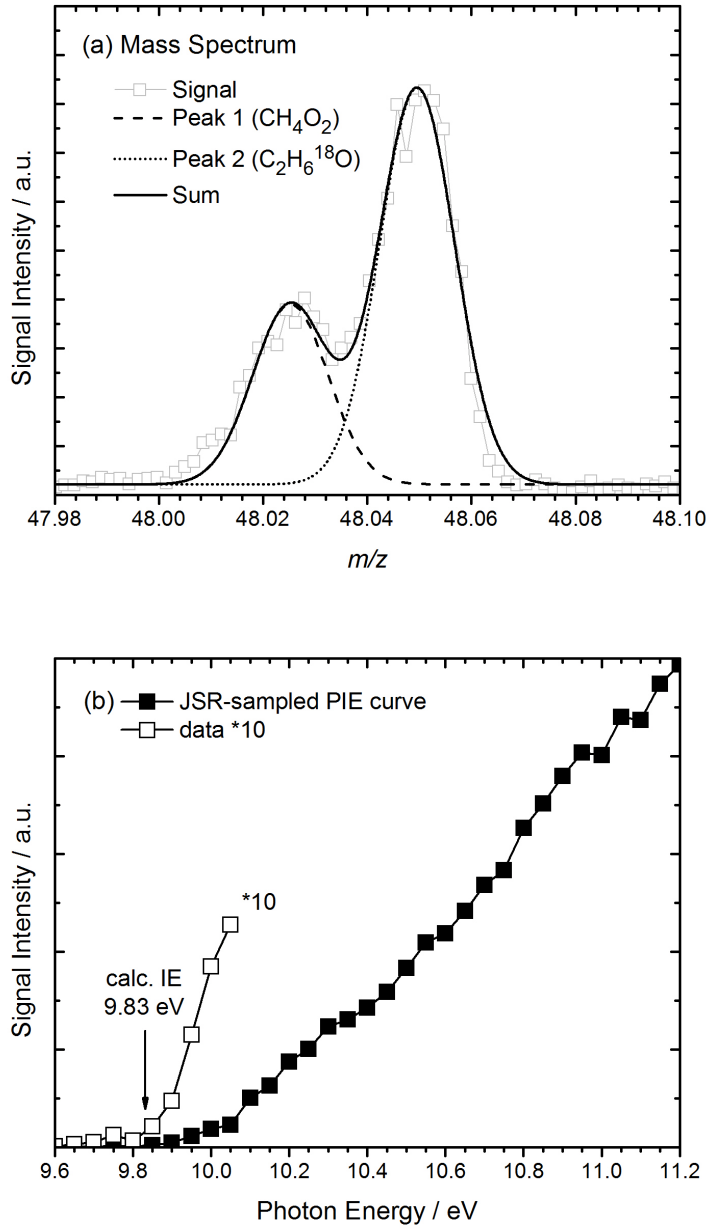

Figure 7:

JSR-sampled photoionization efficiency curve for *m/z* = 60.021 u. Two ionization thresholds can be seen at 10.05(±0.05) eV and 10.8(±0.05) eV. These thresholds match the calculated and known ionization energies of 1,3-dioxetane (*cycl.*-CH_2-O-CH_2-O-) and methyl formate [HC(O)OCH_3] at 10.08 eV and 10.835 eV, respectively. Also shown is the photoionization efficiency curve of methyl formate, which also matches the experimentally observed PIE curve accurately.

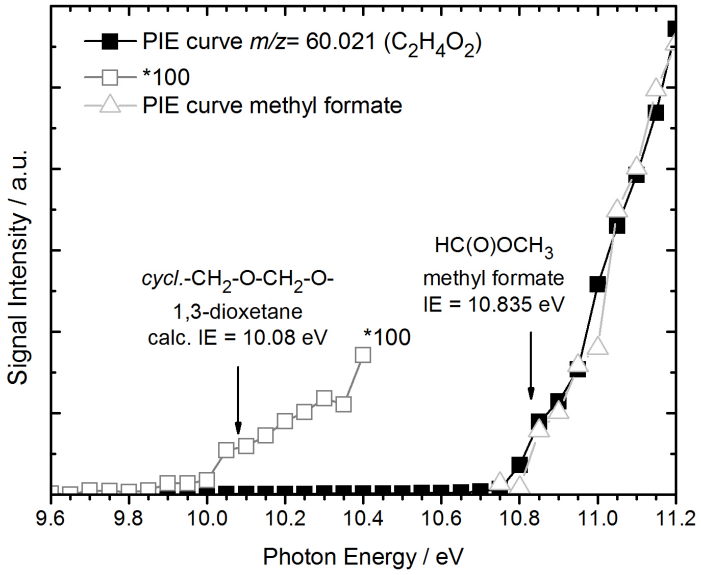

Figure 8:

JSR-sampled photoionization efficiency curve for *m/z* = 92.011 u. The ionization threshold is observed at a photon energy of 9.85 (±0.05) eV. Signals at *m/z* = 91.003 u (-H), 64.016 u (-CO) and 59.013 u (-HO_2) can be assigned as fragments. See text for more details.

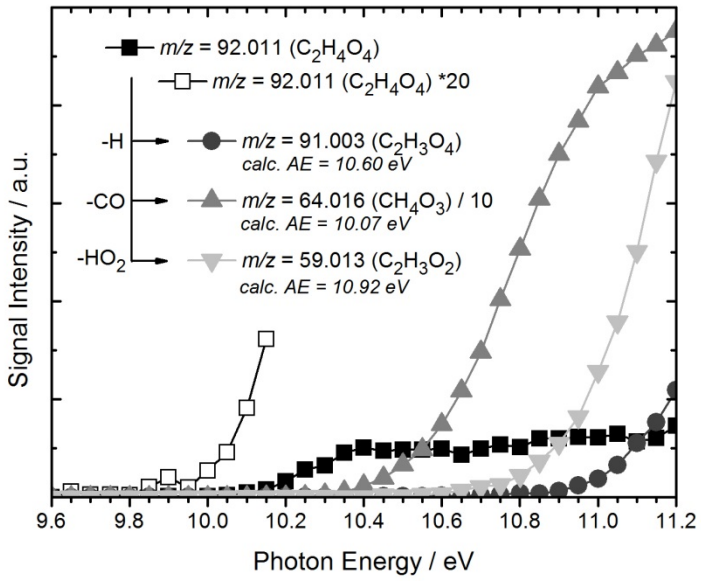

Figure 9:

Conformer-dependent relative ground-state populations and adiabatic ionization energies for $HOOCH_2OCHO$ evaluated at two temperatures.

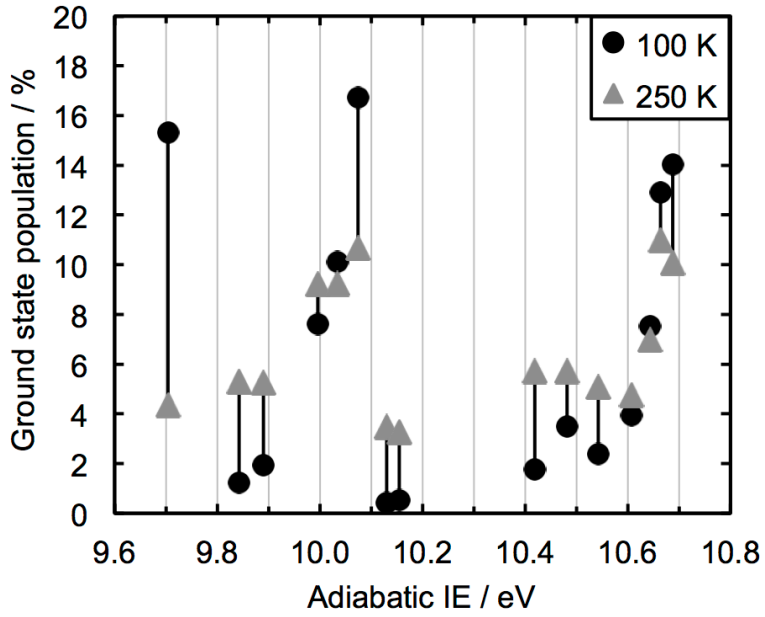

Figure 10:

JSR-sampled photoionization efficiency curve for *m/z* = 74.000 u. An ionization threshold of 10.65(±0.05) eV can be seen, which matches the calculated ionization energy of 10.67 eV very accurately.

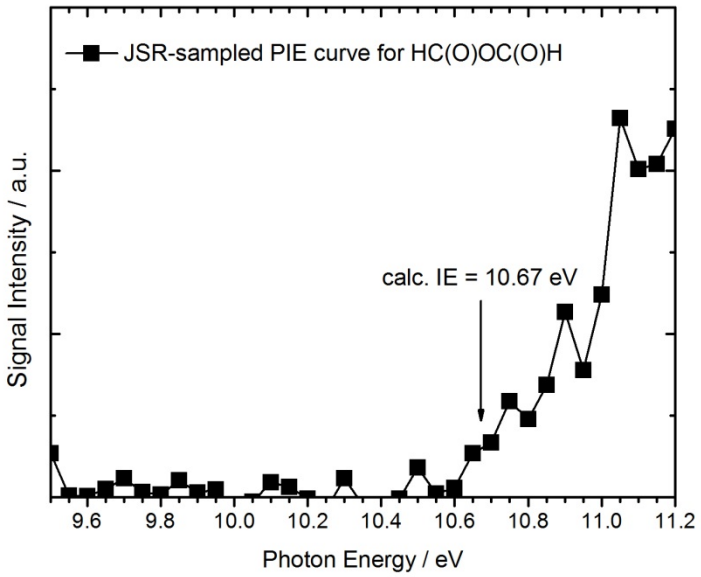

Figure 11:

(a) JSR-sampled, high-resolution mass spectrum at *m/z* = 62 u recorded at 11.2 eV. Two peaks are clearly visible which can be assigned to CH_2O_3 and $C_2H_4{}^{18}OO$. The $C_2H_4{}^{18}OO$ can be identified as the ^{18}O isotopomer of methyl formate. (b) The observed ionization threshold near 10.9(±0.05) eV for CH_2O_3 allows for the identification of performic acid [HC(O)OOH] (calc. IE = 10.87 eV). See text for more details.

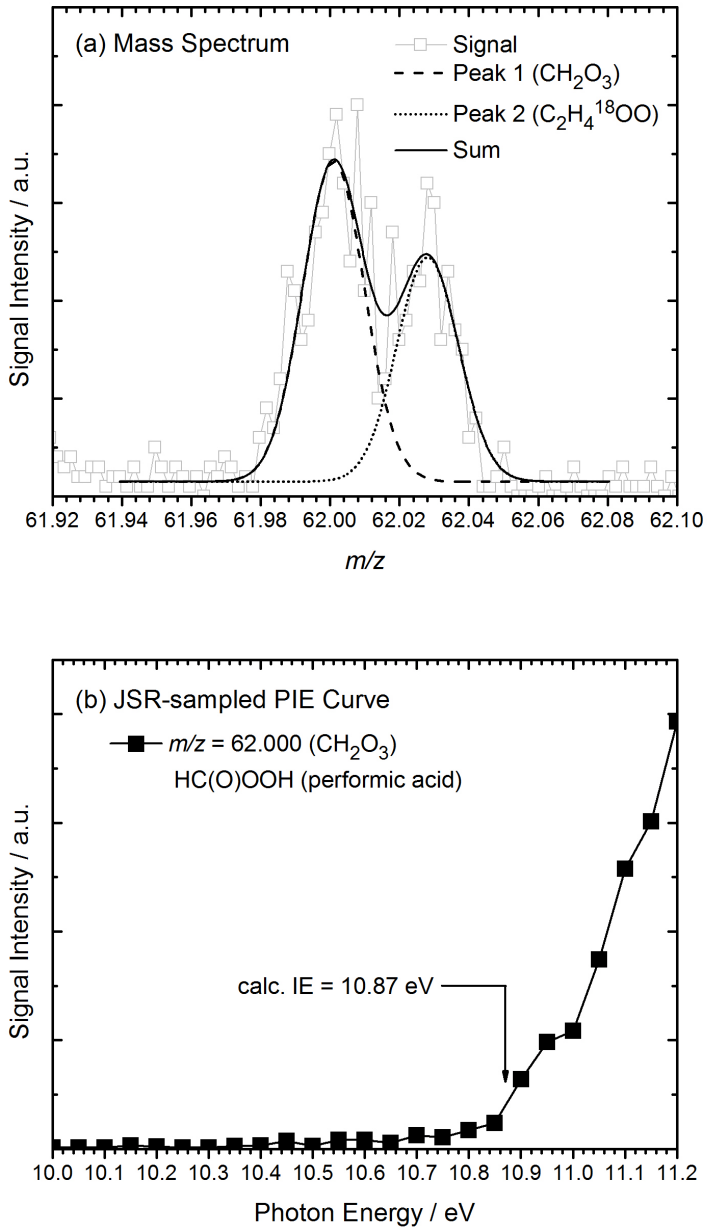

Figure 12:

JSR-sampled PIE curve for m/z = 62.000 u. Signal below 11.2 eV can be attributed to the presence of the performic acid (see Figure 11). A rise in signal intensity near 11.27 eV might be interpreted as due to the presence of carbonic acid [HOC(O)OH], thus potentially providing evidence for the Korcek decomposition mechanism of the keto-hydroperoxide HPMF (see Figure 1). Uncertainty in the experimental data are shown in gray and the arrow indicates the calculated value (and uncertainty) of the *ab initio* calculations.

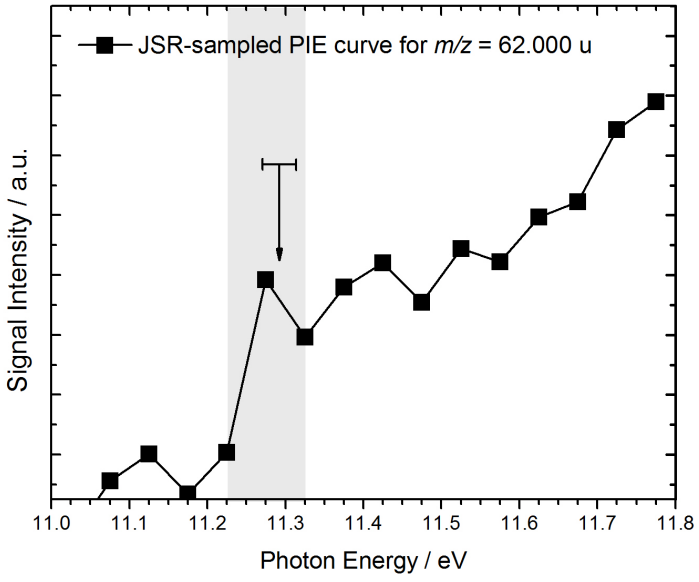
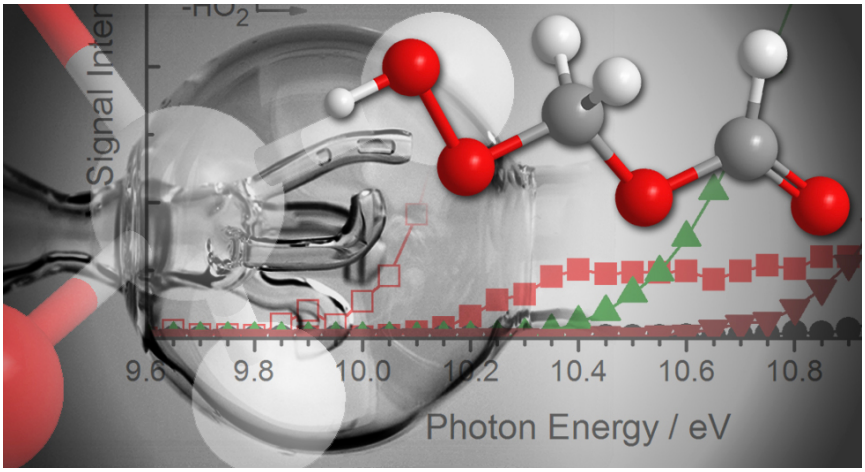
Table-Of-Contents Graphic: